INTERNATIONAL ATOMIC ENERGY AGENCY
UNITED NATIONS EDUCATIONAL, SCIENTIFIC AND CULTURAL ORGANIZATION

INTERNATIONAL CENTRE FOR THEORETICAL PHYSICS
34100 TRIESTE (ITALY) - P.O.B. 586 - MIRAMARE - STRADA COSTIERA 11 - TELEPHONE: 2240-1
CABLE: CENTRATOM - TELEX 460392 - I

SMR/459- 18

SPRING COLLEGE IN CONDENSED MATTER ON 'PHYSICS OF LOW-DIMENSIONAL SEMICONDUCTOR STRUCTURES' (23 April - 15 June 1990)

BACKGROUND INFORMATION

Fabio BELTRAM
AT&T Bell Laboratories
600 Mountain Avenue
Murray Hill, NJ 07974-2070
U.S.A.

Ann. Rev. Mater. Sci. 1986. 16: 263–91

COMPOSITIONALLY GRADED SEMICONDUCTORS AND THEIR DEVICE APPLICATIONS

Federico Capasso

AT&T Bell Laboratories, Murray Hill, New Jersey 07974

Introduction

This paper reviews the electronic transport properties of compositionally graded materials. Band gap grading is a powerful tool for engineering the energy band diagram of a device and thus modifying its electrical transport properties (band gap engineering) (1). The most interesting property, which has far reaching consequences for devices made of these materials, is that electrons and holes experience different electric forces so the transport properties of the two types of carriers can be independently tuned.

With the advent and rapid development of molecular beam epitaxy (MBE) (2) in recent years, graded-gap materials can presently be grown with controlled compositional variations over distances of $\lesssim 100$ Å. In addition, different functional forms of grading (linear, parabolic, etc.) can be obtained by accurately controlling the temperature and/or the opening of the cells in the MBE system. High electron velocities ($> 10^7$ cm/sec) have recently been measured in heavily doped p-type graded-gap $Al_xGa_{1-x}As$.

Ultrahigh-speed phototransistors and transistors with a graded-gap base have been reported. Heterojunction bipolar transistors (HBT's) with a graded emitter-base interface have also been studied in different material systems; for example, parabolic-grading eliminates the collector-emitter offset voltage and maximizes the injection efficiency. Unipolar single and multiple sawtooth graded-gap structures have shown interesting physical properties and device applications. For example, because of the lack of reflection symmetry, sawtooth superlattices can be electrically polarized or used as rectifying elements. Grading of the high field region in avalanche photodiodes has been used to enhance the ionization rates ratio. One of the most exciting recent applications of graded materials is the "staircase"

0084–6600/86/0801–0263$02.00

potential, which can be used as a solid-state photomultiplier and a repeated velocity overshoot device.

Quasi-Electric Fields in Graded-Gap Materials

Kroemer (3) first considered the problem of transport in a graded-gap semiconductor. As a result of compositional grading, electrons and holes experience "quasi-electric" fields, F, of different intensities,

$$F_e = -\frac{dE_c}{dz}$$

$$F_h = +\frac{dE_v}{dz}, \qquad 1.$$

where $E_c(z)$ and $E_v(z)$ are the conduction and valence band edges. In addition, the forces resulting from these fields push electrons and holes in the same direction. This is illustrated in Figure 1*a* for the case of an intrinsic material. Such a graded material can be thought of as a stack of many isotype heterojunctions of progressively varying band gap. If the conduction and valence band edge discontinuities ΔE_c and ΔE_v of such heterojunctions are known and depend little on the alloy composition (as in the case of $Al_xGa_{1-x}As$ heterojunctions), then one can also expect that for the structure in Figure 1*a* the ratio of the quasi-electric fields F_e/F_h will be equal to $\Delta E_c/\Delta E_v$.

For a p-type graded-gap material the situation is different; the energy band diagram is shown in Figure 1*b*. The valence band edge is now horizontal so no effective field acts on the holes, while the effective field for the electrons is $F_e = -dE_g/dz$, which can be significantly greater than in the intrinsic case. In other words, all the band gap grading is transferred to the conduction band. This can be interpreted physically using the following heuristic argument.

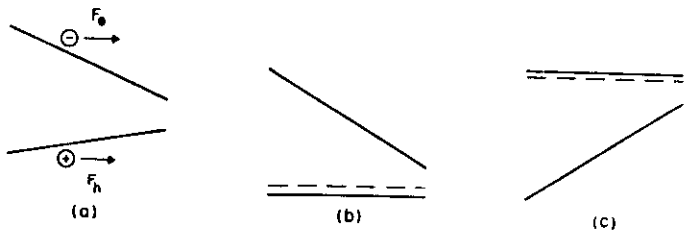

Figure 1 Energy band diagram of compositionally graded materials: (*a*) intrinsic, (*b*) p-type, and (*c*) n-type.

Consider the effect of p-type doping on an initially intrinsic material of the type in Figure 1*a*. The acceptor atoms will introduce holes, which under the action of the valence band quasi-electric field will be spatially separated from their negatively ionized parent acceptor atoms. This separation produces an electrostatic (space-charge) field. Holes accumulate (on the right-hand side of Figure 1*b*) until this space-charge field equals the magnitude of, and cancels, the hole quasi-electric field, F_h, thus achieving the thermodynamic equilibrium configuration (flat valence band) of Figure 1*b*. Note, however, that as a result of this process the equilibrium hole density is spatially nonuniform. The electrostatic field of magnitude $|dE_v/dz|$ produced by the separation of holes and acceptors adds instead to the conduction band quasi-electric field to give a total effective field acting on an electron of

$$F_e = -\left(\frac{dE_c}{dz} + \frac{dE_v}{dz}\right) = -\frac{dE_g}{dz} \qquad 2.$$

Thus in a p-type material the conduction band field is made up of a nonelectrostatic (quasi-electric field) and an electrostatic (space-charge) contribution.

For an n-type material the same kind of argument can be applied to electrons; which yields the band diagram of Figure 1*c* and to the same effective field acting on the hole as given by Equation 2. Consider, for example, the case of an $Al_xGa_{1-x}As$ graded-gap p-type semiconductor. If we recall that in an $Al_xGa_{1-x}As$ heterojunction 62% of the band gap difference is in the conduction band (4), it follows that 62% of the effective conduction band field $F = -dE_g/dz$ will be quasi-electric in nature and the rest (38%) electrostatic. The opposite occurs in the case of an n-type $Al_xGa_{1-x}As$ graded material, where 62% of the valence band effective field is electrostatic in nature.

So far we have only considered quasi-electric fields arising from band gap grading. When the composition of the alloy is changed, however, the effective masses m_e^* and m_h^* of the carriers also change, giving rise to additional quasi-electric fields for electrons and holes. These are given, in the case of intrinsic materials (5), by

$$F_e = \frac{d}{dz}\left[\frac{3}{2}kT \ln (m_e^*/m_0)\right] \qquad 3.$$

$$F_h = \frac{d}{dz}\left[\frac{3}{2}kT \ln (m_h^*/m_0)\right]. \qquad 4.$$

In the case of n- and p-type graded-gap materials one can repeat the previous reasoning and obtain the following expression for the quasi-field due to effective mass gradients:

$$F_{n,p} = \frac{d}{dz}\left[\frac{3kT}{4} \ln (m_e^* m_h^*/m_0^2)\right]. \qquad 5.$$

The quasi-electric fields in direct-band-gap-graded composition $Al_xGa_{1-x}As$ are primarily due to band gap grading; the quasi-electric fields due to the effective mass gradients are negligible in this case (5). However, effective mass gradients can make a substantial contribution to the quasi-electric field for $Al_xGa_{1-x}As$ graded materials in which the composition x is varied through the direct-indirect transition at $x = 0.45$. This is because the effective mass of the electron varies by about one order of magnitude in the direct-indirect transition region. Similar considerations are also thought to apply to other III–V alloys.

Electron Velocity Measurements

Quasi-electric fields are particularly important because they can be used to enhance the velocity of minority carriers that would otherwise move by diffusion (a relatively slow process) rather than by drift. In fact, Kroemer (3) first proposed the use of a graded-gap p-type layer (Figure 1*b*) for the base of a bipolar transistor to reduce the minority carrier (electron) transit time in the base. Recently Levine et al (6, 7), using an all-optical method, measured for the first time the electron velocity in a heavily p^+-doped compositionally graded $Al_xGa_{1-x}As$ layer grown by molecular beam epitaxy.

The energy band diagram of the sample is sketched in Figure 2 along with the principle of the experimental method. The measurement technique is a "pump and probe" scheme. The pump laser beam, transmitted through one of the AlGaAs window layers, is absorbed in the first few thousand angstroms of the graded layer. Optically generated electrons under the influence of the quasi-electric field drift towards the right in Figure 2 and accumulate at the end of the graded layer. This produces a change in the refractive index at the interface with the second window layer. This refractive index variation produces a reflectivity change that can be probed with the counter-propagating laser beam. This reflectivity change is measured as a function of the delay between pump and probe beams using phase-sensitive detection techniques. The reflectivity data (6) are shown in Figure 3 for a sample with a 1-μm-thick transport layer graded from $Al_{0.1}Ga_{0.9}As$ to GaAs and doped to $p \cong 2 \times 10^{18}$ cm^{-3}. This corresponds to a quasi-electric field of 1.2 kV/cm. The laser pulse

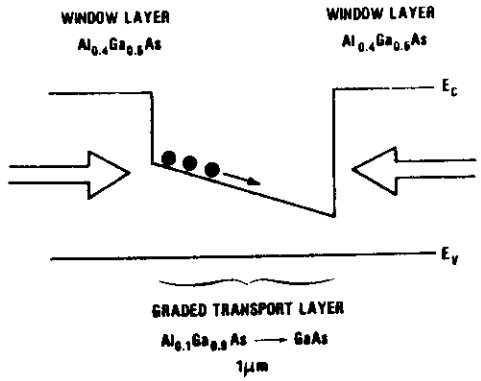

Figure 2 Band diagram of sample used for electron velocity measurements and schematic illustration of the pump-and-probe measurement technique.

width was 15 ps, and the time zero in Figure 3 represents the center of the pump pulse as determined by two photon absorption in a GaP crystal cemented near the sample. The approximate transit time is given by the shift of the half height of the reflectivity curve from zero, which is $\tau = 33$ ps. The drift length is taken as the thickness of the graded layer

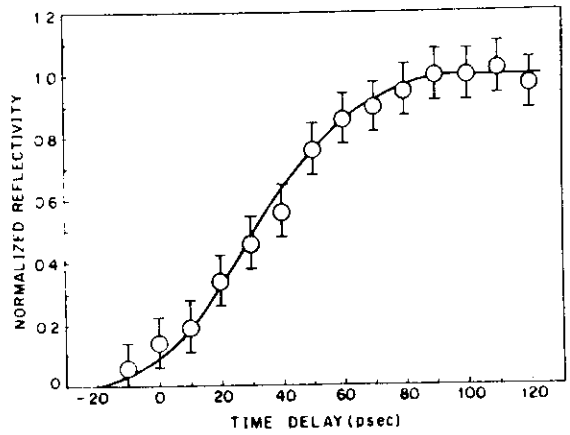

Figure 3 Normalized experimental results for pump-induced reflectivity change versus time delay obtained in 1-μm-thick, graded-gap, p⁺ AlGaAs at a quasi-electric field $F = 1.2$ kV/cm. (From Reference 6.)

minus the absorption length of the pump beam ($1/\alpha \cong 2500$ Å), and one finds a minority carrier velocity of $v \approx (L - \alpha^{-1})/\tau \approx 2.3 \times 10^6$ cm/sec. In this relatively thick sample carrier diffusion is important and causes a spread in the electron arrival time at the end of the sample, which is roughly the rise time of the reflectivity curve from 10 to 90%, i.e. 63 ps.

It is interesting to note that the drift mobility obtained from the measurement is $\mu_0 = v_s/F = 1900$ cm²/V sec, which is comparable with the usual mobility of 2200 cm²/V sec at the doping level of the graded layer in GaAs.

Electron velocity measurements were also made in a 0.42-μm-thick, strongly graded ($F_e = 8.8$ kV/cm), highly doped ($p = 4 \times 10^{18}$ cm⁻³) $Al_xGa_{1-x}As$ layer graded from $Al_{0.3}Ga_{0.7}As$ to GaAs. A transit time of only 1.7 ps was measured, more than an order of magnitude shorter than that for $F = 1.2$ kV/cm, which corresponds to a velocity of roughly $v_s \cong 2.5 \times 10^7$ cm/sec (7). The velocity can be obtained rigorously and accurately (±10% error) from the reflectivity data, by solving the drift diffusion equation and taking into account the effects of the pump absorption length (especially important in the thin sample) and the partial penetration of the probe beam into the graded material. If one includes all these effects, one finds that the reflectivity data can be fitted using only one adjustable parameter, the electron drift velocity (7). This velocity is $v_s = 2.8 \times 10^6$ cm/sec for $F = 1.2$ kV/cm and $p = 2 \times 10^{18}$ cm⁻³, and $v_s = 1.8 \times 10^7$ cm/sec for $F = 8.8$ kV/cm and $p = 4 \times 10^{18}$ cm⁻³.

We see that when we increase the quasi-electric field from 1.2 to 8.8 kV/cm (a factor of 7.3) the velocity increases from 2.8×10^6 to 1.8×10^7 cm/s (a factor of 6.4). That is, we observe the approximate validity of the relation $v = \mu F$. Using $\mu = 1700$ cm²/Vs (for $p = 4 \times 10^{18}$ cm⁻³) we calculate $v = 1.5 \times 10^7$ cm/s for $F = 8.8$ kV/cm, which is in reasonable agreement with the experimental results. The measured velocity of 1.8×10^7 cm/s (in the quasi-electric field) is significantly larger than that of undoped GaAs, in which $v = 1.2 \times 10^7$ cm/s for an ordinary electric field of $F = 8.8$ kV/cm. Our measured high velocity is comparable to the peak velocity reached in GaAs for $F = 3.5$ kV/cm before the transfer from the Γ to the L valley occurs. Our measured velocity is also comparable to the maximum possible phonon-limited velocity in the Γ minimum of GaAs. This is given by $v_{max} = [(E_p/m^*)\tanh(E_p/2kT)]^{1/2} = 2.3 \times 10^7$ cm/s, where $E_p = 35$ meV is the optical phonon energy and the effective mass $m^* = 0.067\, m_0$.

This high velocity can be understood without reference to transient effects because the transit time is much larger than the momentum relaxation time of 0.3 ps. The high velocity results from the fact that the electrons spend most of their time in the high velocity central Γ valley rather than in the low velocity L valley. This may result from the injected

electron density being so much less than the hole doping density that strong hole scattering can rapidly cool the electrons without excessively heating the holes. Furthermore, the electrons remain in the Γ valley throughout their transit across the graded layer since the total conduction band edge drop ($\Delta E_g = 0.37$ eV) is comparable to the GaAs Γ–L separation ($\Delta E_{\Gamma L} = 0.33$ eV), and therefore they do not have sufficient excess energy for significant transfer to the L valley.

High-Speed Graded-Base Transistors

The first device to utilize the high electron velocity found in p-type graded materials was reported by Capasso et al (8). The structure was a phototransistor with an AlGaAs graded-gap base with a quasi-electric field of about 10^4 kV cm. The device was grown by molecular beam epitaxy on a Si-doped ($\approx 4 \times 10^{18}$ cm^{-3}), n$^+$-type GaAs substrate. A buffer layer of n$^+$-type GaAs was grown first, followed by a Sn-doped, n-type ($\approx 10^{15}$ cm^{-3}), 1.5-μm-thick GaAs collector layer. The 0.45-μm-thick base layer was compositionally graded from GaAs (on the collector layer side) to $Al_{0.20}Ga_{0.80}As$ ($E_g = 1.8$ eV) and was heavily doped with Be ($p^+ \cong 5 \times 10^{18}$ cm^{-3}). The abrupt wide gap emitter consisted of an $Al_{0.45}Ga_{0.55}As$ ($E_g = 2.0$ eV), 1.5-μm-thick, window layer n-doped with Sn in the range of 2×10^{15} to 5×10^{15} cm^{-3}. Figure 4*b* shows the energy band diagram of the phototransistor.

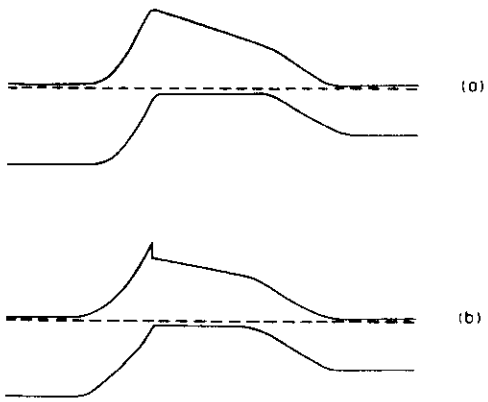

Figure 4 Band diagram of graded-gap base bipolar transistor (*a*) with graded emitter-base interface, and (*b*) with ballistic launching ramp for even higher velocity in the base.

To study the effect of grading in the base on the speed of the device, 4-ps laser pulses were used. The wavelength ($\lambda = 6400$ Å) was chosen so that the light could only be absorbed in the base layer. The incident power was kept relatively high (100 mW) to minimize the effective emitter charging time. Under these conditions the speed-limiting factors are the RC time constant and the base transit time. Figure 5 shows the pulse response of the device as monitored by a fast sampling scope. In the lower part of Figure 5 the response was signal averaged; note the symmetrical rise and fall time and the absence of long tails, which are normally very difficult to achieve in picosecond photodetectors. From the observed 10–90% response time of 30 ps, a sum-of-squares approximation was used to estimate an intrinsic detector response time of about 20 ps. In the absence of a quasi-electric field in the heavily doped p$^+$ base, a broadened response followed by a tail with a square root of time dependence (due to slow diffusion) is expected. The diffusion time t_D is given by $W^2/2D$, where W is the base thickness and D is the diffusion coefficient. For a GaAs phototransistor with a base of $p^+ = 10^{18}$ cm^{-3} D is approximately 16 cm^2/s. In our structure D is likely to be smaller because AlGaAs has a lower mobility than GaAs, and because of the higher doping. For our structure $t_D \geq 50$ ps. The fact that the expected broadening is not observed indicates that the quasi-electric field in the base sweeps out the electrons in a time much shorter than the diffusion time. From the velocity measurements previously discussed we know that the base transit time is about 2 ps, which is indeed much less than t_D. Thus the pulse response of this device is consistent with Kroemer's prediction (3) and is the first experimental verification of this effect (8).

Finally, the combination of the graded-gap base and the abrupt wide gap emitter (Figure 4*b*) suggests a new high-speed ballistic transistor (8, 9). In fact, the conduction band discontinuity can be used to ballistically launch electrons into the base with a high initial velocity; the quasi-electric field in the base will maintain an average velocity substantially higher than 10^7 cm/s. If no electric field were introduced in the base, ballistic launching alone, using the abrupt base emitter heterojunction, would not be sufficient to achieve a very high velocity in the base because collisions with plasmons or coupled plasmon-phonon modes in the heavily doped base would rapidly relax the initial forward momentum and velocity. It is sufficient for an initial high velocity that the conduction band discontinuity used for the launching be a few kT (typically 50 mV at 300 K).

Recently the first bipolar transistor with a compositionally graded base was reported (10, 11). Incorporation of a graded-gap base gives much faster base transit times because of the induced quasi-electric field for electrons, which allows a valuable tradeoff against the base resistance. To understand this last point consider a base of width W linearly graded from

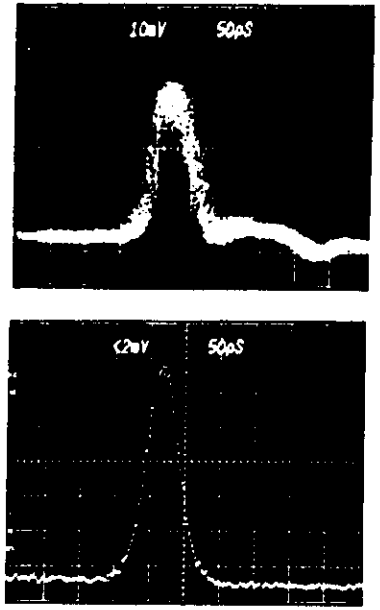

Figure 5 Pulse response of graded-gap base AlGaAs/GaAs phototransistor to a 4-ps laser pulse displayed on a sampling scope (*top*), and after signal averaging the sampling scope signal (*bottom*). (From Reference 8.)

one alloy with a band gap of E_{g1} to another with a band gap of E_{g2}. The quasi-electric field for electrons $(E_{g1}-E_{g2})/eW$ results in a base transit time (neglecting diffusion effects) of

$$\tau_b' = \frac{eW^2}{\mu(E_{g1}-E_{g2})}. \qquad 6.$$

We have made use of the experimental fact that the velocity in the graded base nearly equals μF_e, where F_e is the quasi-electric field (7). This time must be compared with the diffusion-limited base transit time of a transistor with an ungraded GaAs base of the same thickness and doping level

$$\tau_b = \frac{W^2}{2D}, \qquad 7.$$

where D is the ambipolar diffusion coefficient. If we compare Equations 6 and 7 and use the Einstein relationship $D = \mu kT/e$, we find that the base

transit time is shortened by the factor

$$\frac{\tau_b'}{\tau_b} = \frac{E_{g1}-E_{g2}}{2kT}. \qquad 8.$$

using a graded-gap base. Although Equation 8 is rigorous only in the limit $E_{g1}-E_{g2} \gg kT$, it can be employed as a useful "rule of thumb" in cases where $E_{g1}-E_{g2}$ is several times kT. Thus the band gap difference must be made as large as possible without exceeding the intervalley energy separation $\Delta E_{\Gamma L}$, which would greatly reduce the electron velocity. Using $E_{g1}-E_{g2} = 0.2$ eV, the transit time is reduced by a factor of about four at 300 K relative to an ungraded base of the same thickness. This allows a valuable tradeoff against the base resistance (R_b), since the base thickness can be increased to reduce R_b, while still keeping a reasonable base transit time. Finally, an added advantage of the quasi-electric field is the increased base transport factor that comes about because the short transit time reduces minority carrier recombination in the base.

Devices (10) grown by MBE on an n^+ substrate had a 1.5-μm GaAs buffer layer followed by a 5000-Å-thick collector doped to $n \cong 5 \times 10^{16}$ cm^{-3}. The p-type (2×10^{18} cm^{-3}) base was graded from $Ga_{0.98}Al_{0.02}As$ to $Ga_{0.8}Al_{0.2}As$ over 4000 Å. This grading corresponds to a field of about 5.6 kV/cm. The lightly doped ($n \cong 2 \times 10^{16}$ cm^{-3}), wide gap emitter consisted of an $Al_{0.35}Ga_{0.65}As$ layer 3000 Å thick and a region adjacent to the base graded from $Ga_{0.8}Al_{0.2}As$ to $Ga_{0.65}Al_{0.35}As$ over 500 Å. This corresponds to a base/emitter energy gap difference of approximately 0.18 eV. This grading removes a large part of the conduction band spike, allowing most of the band gap difference to fall across the valence band and blocking the unwanted injection of holes from the base (12). Figure 4*a* shows the energy band diagram of the structure in the equilibrium (unbiased) configuration.

These devices had a current gain of 35 at a base current of 1.6 mA, and the collector characteristics were nearly flat with minimum collector-emitter offset voltage. More recently, high current gain, graded base bipolars with good high-frequency performance have been reported (Malik et al 12). The base layer was linearly graded over 1800 Å, from $x = 0$ to $x = 0.1$, which resulted in a quasi-electric field of 5.6 kV/cm, and was doped with Be to $p = 5 \times 10^{18}$ cm^{-3}. The emitter-base junction was graded over 500 Å from $x = 0.1$ to $x = 0.25$ to enhance hole confinement in the base. The 0.2-μm-thick $Al_{0.25}Ga_{0.75}As$ emitter and the 0.5-μm-thick collector were doped n-type at 2×10^{17} cm^{-3} and 2×10^{16} cm^{-3}, respectively. The $Al_xGa_{1-x}As$ layers were grown at a substrate temperature

of 700 C. It was found that this high growth temperature resulted in better $Al_xGa_{1-x}As$ quality, as determined by photoluminescence. However, it is known that significant Be diffusion occurs during MBE growth at high substrate temperatures and at high doping levels ($p > 10^{18}$ cm^{-3}). Secondary ion mass spectrometry (SIMS) data also indicated that the p-n junction was misplaced into the wide band gap emitter at 700 C. It was determined empirically that the insertion of an undoped setback layer of 200–500 Å between the base and emitter compensated for the Be diffusion and resulted in significantly increased current gains. Zn diffusion was used to contact the base and provided a low base contact resistance.

With a dopant setback layer in the base of 300 Å the maximum differential dc current gain was 1150, obtained at a collector current density of $J_c = 1.1 \times 10^3$ Acm^{-2}, a higher gain than previously reported for graded-gap base HBT's. These gains can be compared with those found in previous work, which were consistently < 100 in HBT's without the set-back layer (10, 11). Several transistor wafers were processed with undoped setback layers in the base of 200–500 Å, and all exhibited greater current gains.

Graded-gap base HBT's were fabricated for high-frequency evaluation using the Zn diffusion process. A single 5-μm-wide emitter strip contact with dual adjacent base contacts was used. The areas of the emitter and collector junctions were approximately 2.3×10^{-6} cm^2 and 1.8×10^{-5} cm^2, respectively. The transistors were wire bonded in a microwave package, and automated *s*-parameter measurements were made with an HP 8409 network analyzer. The transistor has a current gain cutoff frequency of $f_T \approx 5$ GHz and a maximum oscillation frequency of $f_{max} \approx 2.5$ GHz. Large signal pulse measurements indicated rise times of $\tau_r \simeq 150$ ps and pulsed collector currents of $I_c > 100$ mA, suitable for high-current laser driver applications.

Emitter Grading in Heterojunction Bipolar Transistors

The essential feature of the heterojunction bipolar transistor is the use of part of the energy band gap difference between the wide band gap emitter and the base to suppress hole injection. This allows the base to be more heavily doped than the emitter, which leads to the low base resistance and low emitter-base capacitance necessary for high-frequency operation while still maintaining a high emitter injection efficiency (9). In this section we discuss in detail the grading problem in heterojunction bipolars. The performances of recently developed $Al_{0.48}In_{0.52}As/Ga_{0.47}In_{0.53}As$ bipolars with graded and ungraded emitters are compared (13), and the optimum grading of the emitter is discussed.

Most of the work on MBE-grown heterojunction bipolar transistors has concentrated on the AlGaAs/GaAs system. Recently the first vertical Npn $Al_{0.48}In_{0.52}As/Ga_{0.47}In_{0.53}As$ heterojunction bipolar transistors grown by MBE with high current gain have been reported by Malik et al (13). The (Al,In)As/(Ga,In)As layers were grown by molecular beam epitaxy (MBE) lattice-matched to an Fe-doped semi-insulating InP substrate. Two HBT structures were grown: the first with an abrupt emitter of $Al_{0.48}In_{0.52}As$ on a $Ga_{0.47}In_{0.53}As$ base, and a second with a graded emitter comprising a quaternary layer of AlGaInAs 600 Å wide and linearly graded between the two ternary layers. Grading from $Ga_{0.47}In_{0.53}As$ to $Al_{0.48}In_{0.52}As$ was achieved by simultaneously lowering the Ga and raising the Al oven temperatures in such a manner as to keep the total Group III flux constant during the transition. It should be noted that this is the first use of a graded quaternary alloy in a device structure.

The energy band diagram for the abrupt and graded emitter transistors are shown in Figure 6*a* and *b*, respectively. The effect of the grading is to eliminate the conduction band notch in the emitter junction. This in turn

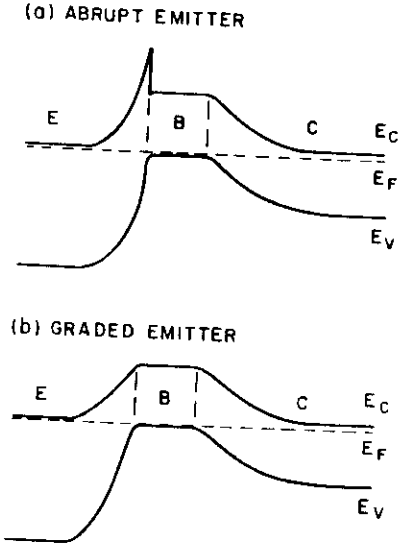

Figure 6 Band diagrams under equilibrium of heterojunction bipolar with (*a*) an abrupt emitter and (*b*) a graded emitter. Note that the conduction band notch is eliminated through the use of a graded emitter and the increase of the emitter-base valence band barrier. (From Reference 13.)

leads to a larger emitter-base valence band difference under forward bias injection. The following material parameters were used in both types of transistors. The $Al_{0.48}In_{0.52}As$ emitter and $Ga_{0.47}In_{0.53}As$ collector were doped n-type with Sn at levels of 5×10^{17} cm^{-3} and 5×10^{16} cm^{-3}, respectively. The $Ga_{0.47}In_{0.53}As$ base was doped p-type with Be to a level of 5×10^{18} cm^{-3}. Recent experimental determination of the band edge discontinuities in the $Al_{0.48}In_{0.52}As/Ga_{0.47}In_{0.53}As$ heterojunction indicates $\Delta E_c \cong 0.50$ eV and $\Delta E_v \cong 0.20$ eV (14). This value of ΔE_c is large enough to allow the use of an abrupt $Al_{0.48}In_{0.52}As/Ga_{0.47}In_{0.53}As$ emitter at 300 K. Nevertheless, a current gain increase by a factor of two (from $\beta = 200$ to $\beta = 400$) is achieved through the use of the graded-gap emitter, which is attributed to a larger valence band difference between the emitter and base under forward bias injection.

The common emitter characteristic of HBT's exhibits a relatively large collector-emitter offset voltage. This voltage is equal to the difference between the built-in potential for the emitter-base p-n junction and that of the base-collector p-n junction. Therefore no such offset is present in homojunction Si bipolars.

We have recently shown that by appropriately grading the emitter near the interface with the base such offset can be reduced and even totally eliminated (15). The other advantage of grading the emitter is of course that the potential spike in the conduction band can be reduced, thus increasing the injection efficiency. The conduction band potential has two components: the electrostatic potential ϕ_{es} equal to V_{bi} (the built-in potential) $- V_{be}$ (the base/emitter voltage), which varies parabolically, and the grading potential ϕ_g. If linear grading is used there is always unwanted structure in the conduction band (spikes or notches, see Figure 7). The "notches" can reduce the injection efficiency by promoting carrier recombination. It has now become obvious that such structures can be eliminated by grading with the complementary function of the electrostatic potential in the emitter region ($1\text{-}\phi_{es}$) over the depletion layer width at a forward bias equivalent to the base band gap (Figure 8). In this case if the base emitter junction is forward biased at 1.42 eV, the two potentials (grading and electrostatic) give rise to a smooth conduction band edge and one attains the flat band condition with a built-in voltage for the base emitter equivalent to the band gap in the base (1.42 eV).

A HBT with such a parabolic grading has been fabricated, using MBE, with a $Ga_{0.7}Al_{0.3}As$ emitter and a GaAs base and collector (15). The emitter/base junction was graded from $x = 0$ to $x = 0.3$ on the emitter side over a distance of 600 Å; the parabolic grading function was approximated by linear grading over nine regions. It was found that collector-emitter offset voltage is very small (about 0.03 V).

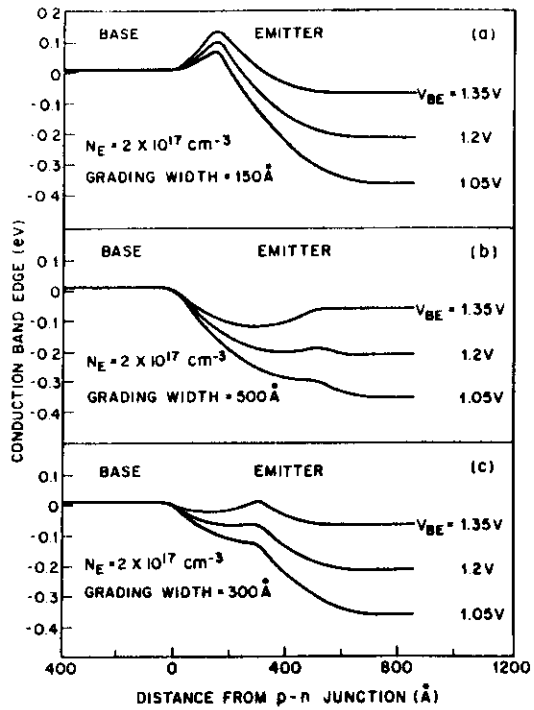

Figure 7 Conduction band edge versus distance from the p$^+$-n base-emitter junction for three different linear grading widths at different base emitter forward bias voltages. (From Reference 15.)

Graded-Gap Lasers, Solar Cells, and Avalanche Photodiodes

If the active layer of a conventional double heterostructure laser is reduced to a thickness where the quantum size effect becomes important, i.e. less than 400 Å, the structure lases at a very high threshold current density because the overlap of the photon and electron populations is very small. To increase this overlap a separate optical cavity with graded composition is grown around the quantum well active layer. Here the electrons are "funnelled" into the quantum well region by the quasi-electric field of the

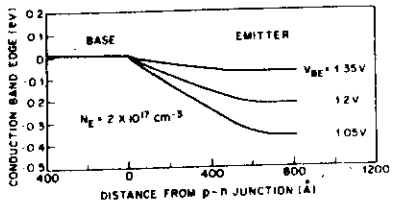

Figure 8 Conduction band edge versus distance from the p⁺-n junction, using a parabolically graded layer 500 Å wide at different forward bias voltages. (From Reference 15.)

graded composition layers and therefore have a higher probability of capture by the quantum well. This device is known as the GRINSCH (graded-index separate confinement heterostructure) laser after Tsang (16), who first combined the quantum well laser (17) with the graded optical confinement region, which had been proposed by Kazarinov & Tsarenkov (18).

In solar cells, band gap grading in the top layer has been used to efficiently collect carriers optically generated near the surface, before they recombine through surface states. High-efficiency $Al_xGa_{1-x}As$-GaAs solar cells have been fabricated by Woodall & Hovel (19) using this scheme.

Graded gaps can also be used to enhance the ratio of ionization coefficients (α/β) in avalanche photodiodes (20). The ionization coefficient $\alpha(\beta)$ is defined as the number of secondary pairs created per unit length along the direction of the field by an electron (hole) by impact ionization. The value α/β plays a crucial role in the signal-to-noise ratio of an avalanche photodiode (21). The α/β ratio must be either very large or very small to minimize the avalanche excess noise.

Recently Capasso et al (20) proposed and demonstrated experimentally a new avalanche detector in which α/β is enhanced with respect to the bulk value of the alloys constituting the graded-gap material. The structure, grown by MBE, consists of a nominally intrinsic region, graded from GaAs to $Al_{0.45}Ga_{0.55}As$ ($E_g = 2.0$ eV) and sandwiched between n^+ and p^+ regions. We demonstrated that the effective α/β ratio of this structure is significantly increased over 1 ($\alpha/\beta \cong 5$–7.5) if the width of the graded layer is $\lesssim 0.5$ μm. The principle of the device is illustrated in Figure 9. The electrons have a lower ionization energy than the holes because they are moving towards lower gap regions. The effect is a significant increase in the α/β ratio when the grading exceeds 1 eV/μm. Another important property of this structure is the soft breakdown, which can lead to much greater gain stability compared to ungraded diodes. This is due to the fact that avalanche multiplication is always initiated in the low gap

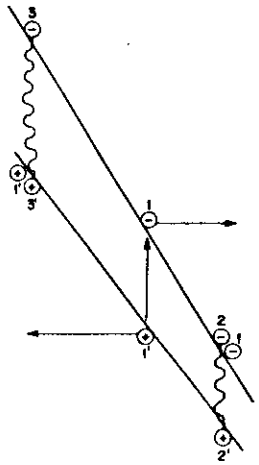

Figure 9 Band diagram of graded band gap avalanche photodiode showing impact ionization by the initial electron-hole pair 1-1'. (From Reference 20.)

regions and then spreads out to the higher gap regions as the electric field is increased.

Multilayer Sawtooth Materials

In this section we examine the electronic transport properties of sawtooth structures obtained by periodically varying the composition of the alloy in an asymmetric fashion. The key feature of such structures is the lack of reflection symmetry (22). This has several important consequences; for example, these devices can be used as rectifying elements or, under suitable conditions, one can optically generate in these structures a macroscopic electrical polarization that gives rise to a cumulative photovoltage across the uniformly doped sawtooth material. In addition, under appropriate bias they give rise to a staircase potential which has several intriguing applications.

RECTIFIERS The basic principle of sawtooth rectifiers, recently demonstrated by Allyn et al (23, 24), is shown in Figure 10. A sawtooth-shaped potential barrier is created by growing a semiconductor layer of graded chemical composition followed by an abrupt composition discontinuity. The adjoining layers, with which contact is made, are of the same conductivity type. In the present case, the barrier material is aluminum gallium arsenide ($Al_xGa_{1-x}As$) in which the aluminum content is graded and the adjoining layers are n-type GaAs. Near zero bias, conduction in the direction perpendicular to the layer is inhibited by the

barrier. When the device is biased in the forward direction (as shown in Figure 10*c*) the voltage drop initially occurs across the graded layer, reducing the slope of the potential barrier, and allowing increased thermionic emission over the reduced barrier. When the applied voltage exceeds the barrier height, the device will conduct completely, as in the case of a Schottky barrier. In the reverse direction (Figure 10*d*) electrons will be attracted to, but inhibited from passing through, the abrupt potential discontinuity at the sharp edge of the sawtooth. The width of the interface and potential discontinuity is known to be only 5–10 Å. Thus, the primary reverse current-carrying mechanism will be tunnelling. The barrier can be either doped or undoped, although depletion of carriers from within the barrier (in the case of doped barriers) leads to band bending, which reduces the equilibrium height and width of the barrier. Multiple sawtooth barriers with five periods were also fabricated (23). These showed a turn-on

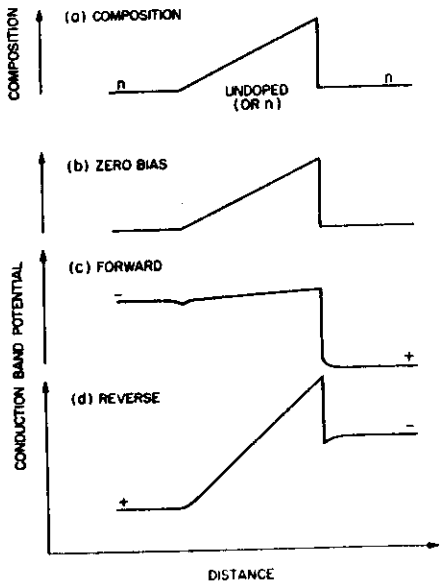

Figure 10 (*a*) Compositional structure of a sawtooth barrier rectifying structure, (*b*) potential distribution for band-edge conduction electrons at zero bias (undoped barrier case), (*c*) potential distribution under forward bias, and (*d*) potential distribution under reverse bias. (From Reference 23.)

voltage equal to five times that of the single barrier, thus demonstrating the additivity of the technique.

ELECTRICAL POLARIZATION EFFECTS IN SAWTOOTH SUPERLATTICES The lack of planes of symmetry in sawtooth superlattice material, compared to conventional superlattices with rectangular wells and barriers, can lead to electrical polarization effects. Recently Capasso et al (25) reported for the first time on the generation of a transient macroscopic electrical polarization extending over many periods of the superlattice. This effect is a direct consequence of the above-mentioned lack of reflection symmetry in these structures.

The energy band diagram of a sawtooth p-type superlattice is sketched in Figure 11*a*, in which we have assumed a negligible valence band offset. The layer thicknesses are typically a few hundred angstroms, and a suitable material is graded-gap $Al_xGa_{1-x}As$. The superlattice is sandwiched between two highly doped p^+ contact regions.

Let us assume that electron-hole pairs are excited by a very short light pulse, as shown in Figure 11*a*. Due to the grading, electrons experience a higher quasi-electric field than do holes. For this reason, and because

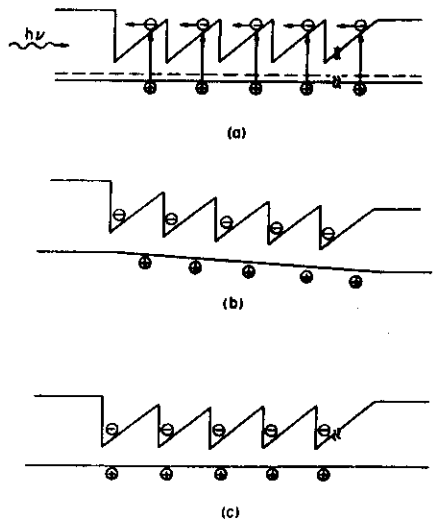

Figure 11 Formation and decay of the macroscopic electrical polarization in a sawtooth superlattice. (From Reference 25.)

of their much higher velocity, electrons separate from holes and reach the low gap side in a subpicosecond time ($\simeq 10^{-13}$ sec). This sets up an electrical polarization in the sawtooth structure, which results in the appearance of a photovoltage across the device terminals (Figure 11*b*). The macroscopic dipole moment and its associated voltage subsequently decay in time by a combination of (*a*) dielectric relaxation and (*b*) hole drift.

The excess hole density decays by dielectric relaxation to restore a flat valence band (equipotential) condition, as illustrated in Figure 11*c*. Note that in this final configuration holes have redistributed to neutralize the electrons at the bottom of the wells. Thus the net negative charge density on the low gap side of the wells decreases with the same time constant as the positive charge packet (the dielectric relaxation time). The other mechanism by which the polarization decays is hole drift caused by the electric field created by the initial spatial separation of electrons and holes.

The graded-gap superlattice structure shown in Figure 11 and the underlying p^+-GaAs buffer layer were grown by MBE. A total of ten graded periods were grown with a period of ≈ 500 Å. The layers are graded from GaAs to $Al_{0.2}Ga_{0.8}As$. A heavily doped GaAs contact layer of ≈ 700 Å was grown on top of the 1-μm-thick $Al_{0.45}Ga_{0.55}$ ($p \approx 5 \times 10^{18}$ cm^{-3}) window layer. Unbiased devices were mounted in a microwave stripline and illuminated with short light pulses (4 ps) of wavelength $\lambda = 6400$ Å. The absorption length is ≈ 3500 Å. In this particular wafer the carrier concentration was 10^{16} cm^{-3}. It was found that the rise time of the pulse response is ≤ 25 ps, while the fall time (at the $1/e$ point) is $\cong 200$ ps. Unlike conventional detectors, the current carried in this photodetector is of a displacement rather than a conduction nature since it is associated with a time-varying polarization. This current, by continuity, equals the conduction current in the external load.

STAIRCASE STRUCTURES Recently Capasso et al introduced the concept of a staircase potential (26-30). This innovative structure has several interesting applications. We shall concentrate on the staircase avalanche photodiode (APD) (1, 26-30) and on the repeated velocity overshoot device (31).

Staircase solid-state photomultipliers and avalanche photodiodes Figure 12*a* shows the band diagram of the graded-gap multilayer material (assumed intrinsic) at zero applied field. Each stage is linearly graded in composition from a low (E_{g1}) to a high (E_{g2}) band gap, with an abrupt step back to low band gap material. The conduction band discontinuity shown accounts for most of the band gap difference, as is typical of many III-V heterojunctions. The materials are chosen for a conduction band discontinuity comparable to or greater than the electron ionization energy E_{ic} in the low gap material following the step. The biased detector is shown in Figure 12*b*. Consider a photoelectron generated near the p^+ contact: The electron does not impact ionize in the graded region before the conduction band step because the net electric field is too low. At the step, however, the electron ionizes and the process is repeated at every stage. Note that the steps correspond to the dynodes of a phototube. Holes created by electron impact ionization at the steps do not impact ionize, since the valence band steps are of the wrong sign to assist ionization and the electric field in the valence band is too low to cause hole-initiated ionization. Obviously holes multiply since at every step both an electron and a hole are created. The gain is $M = (2-\delta)^N$ where δ is the fraction of electrons that do not ionize per stage. The noise per unit bandwidth on the output signal, neglecting dark current, is given by $\langle i^2 \rangle = 2eI_{ph}M^2F$, where I_{ph} is the primary photocurrent and F the avalanche excess noise factor. For the staircase APD F is given by (30)

$$F = 1 + \frac{\delta[1-(2-\delta)^{-N}]}{2-\delta}. \qquad 9.$$

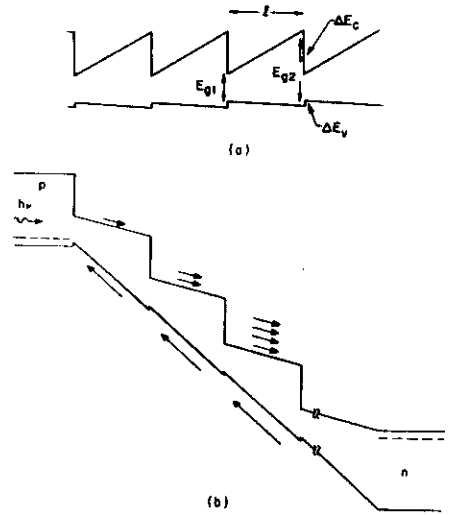

Figure 12 Band diagram of staircase solid-state photomultiplier. The arrows in the valence band simply indicate that holes do not impact ionize. (From Reference 30.)

Note that for small δ, $F \cong 1$ and is practically independent of the number of stages. Thus, the multiplication process is essentially noise free. It is interesting to note that the excess noise of this structure does not follow the McIntyre theory of conventional APD's (21). In a conventional APD the minimum excess noise factor at high gain (> 10) is two if one of the ionization rates is zero. The fact that in the staircase APD the avalanche noise is lower than in the best conventional APD's ($\alpha/\beta = \infty$) can be understood as follows: In a conventional APD the avalanche is more random because carriers can ionize everywhere in the avalanche region, while in the staircase APD electrons ionize at well-defined positions in space (i.e. the multiplication process is more deterministic). Note that, similarly, in a photomultiplier tube the avalanche is essentially noise free ($F \cong 1$).

Finally, the low voltage operation of this device with respect to conventional APD's should be mentioned. For a five stage detector and $\Delta E_c \cong E_{g1} \cong 1$ eV, the applied voltage required to achieve a gain of about 32 is slightly greater than 5 V. Possible material systems for the implementation of the device in the 1.3–1.6 μm region are AlGaAs/GaSb and HgCdTe. In a practical structure one should always leave an ungraded layer immediately after the step having a thickness of the order of a few ionization mean free paths ($\lambda \cong$ 50–100 Å) to ensure that most electrons ionize near the step.

In progress toward the staircase APD, which has not yet been implemented, recently Capasso et al (32) demonstrated experimentally an enhancement of the α/β ($\cong 8$) in an AlGaAs/GaAs quantum well superlattice. The effect has been attributed to the difference between the conduction and valence band discontinuities ($\Delta E_c > \Delta E_v$). Thus electrons enter the well with a higher kinetic energy than holes and have a higher probability of ionizing. Note that the staircase APD is the limiting case of this detector since the whole ionization energy is gained at the band discontinuity. The staircase devices are probably the best example of the band gap engineering concept.

Repeated velocity overshoot devices Another interesting application of staircase potentials has been proposed, the repeated velocity overshoot device (31). This structure offers the potential for achieving average drift velocities well in excess of the maximum steady-state velocity over distances greater than 1 μm. Figure 13*a* shows a general type of staircase potential structure. The corresponding electric field, shown in Figure 13*b*, consists of a series of high field regions of value E_1 and width d superimposed upon a background field E_0. To illustrate the electrical behavior and design considerations for a specific case, we consider electrons in the

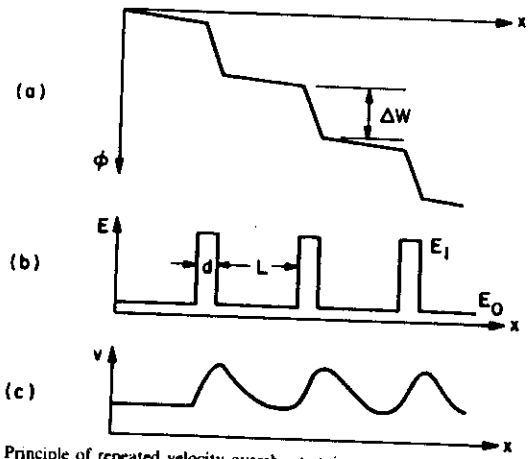

Figure 13 Principle of repeated velocity overshoot staircase potential and corresponding electric field. The ensemble velocity as a function of position is also illustrated. (From Reference 31.)

central valley of GaAs. The background field E_0 is chosen so that the steady-state electron energy distribution is not excessively broadened beyond its thermal equilibrium value, but at the same time the average drift velocity is still relatively high. For GaAs, an appropriate value would be around 2.5 kV/cm. At this field, the steady-state drift velocity is 1.8×10^7 cm/s and fewer than 2% of the electrons reside in the satellite valley. The electron distribution immediately downstream from the high field region is shifted to higher energy by an amount $\Delta W = E_1 d$. (Note that while the distribution is shifted uniformly in energy, it is compressed in momentum in the direction of transport.) We choose d so that the transit time across the high field region is shorter than the mean phonon scattering time, which is about 0.13 ps in GaAs. The energy step ΔW is chosen to maximize the average velocity of the distribution after the step while still keeping most of the distribution below the threshold energy for transfer to the satellite valley. In GaAs, the intervalley separation is about 0.3 eV, so an appropriate value of ΔW would be about 0.2 eV, resulting in an average velocity of approximately 1×10^8 cm/s immediately after the step. The momentum decays rapidly beyond the step due to scattering by polar optical phonons, with the result that the velocity decreases roughly linearly with distance, as shown in Figure 13*c*. During this time the distribution is broadened considerably in momentum. After the momen-

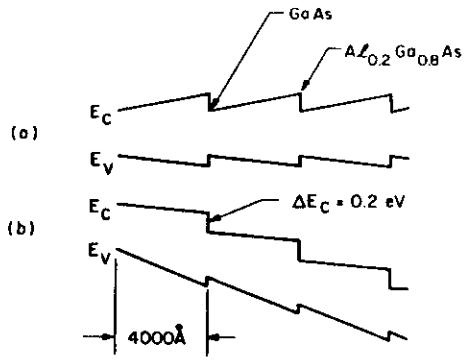

Figure 14 Band diagram of a graded-gap repeated velocity overshoot device. (From Reference 31.)

tum (and velocity) have relaxed, the distribution requires additional time to relax to its original energy. Thus, the spacing L between high field regions must be large enough to allow sufficient cooling of the electron distribution before another overshoot can be attempted. This is necessary to avoid populating the high mass satellite valleys. The effect of the resulting repeated velocity overshoot shown in Figure 13*c* is that average drift velocities greater than the maximum steady-state velocity can be maintained over very long distances. A practical way to achieve this device with graded-gap materials is shown in Figure 14.

Superlattice Band-Gap Grading and Pseudo-Quaternary Alloys

The growth of graded-gap structures of very short period represents a real challenge for the MBE crystal grower. In addition to a computer-controlled MBE system, new techniques to achieve very short distance compositional grading are necessary. One such technique is the recently introduced pulsed-beam method (33). This technique can be used, for example, to grow a variable gap alloy by alternately opening and closing the shutters of aluminum and gallium ovens. The result is an AlAs/GaAs superlattice with an ultrathin fixed period (≈ 20 Å) but a varying ratio of AlAs to GaAs layer thicknesses. The local band gap is therefore that of the alloy corresponding to the local average composition, determined by the thicknesses of the AlAs and the GaAs. Since the period of the superlattice is much smaller than the de Broglie wavelengths of the carriers, the material

behaves basically like a *variable gap ordered alloy*. Such techniques have been used recently to grow parabolic quantum wells (34) (Figure 15).

Another interesting example of superlattice alloys are the pseudo-quaternary materials introduced by Capasso et al (35). Such artificial structures are capable of conveniently replacing GaInAsP semiconductors in a variety of applications. The concept of a pseudo-quaternary GaInAsP semiconductor is easily explained. Consider a multilayer structure of alternated $Ga_{0.47}In_{0.53}As$ and InP. If the layer thicknesses are sufficiently thin (typically a few tens of angstroms) one is in the superlattice regime. As a result, this novel material has its own band gap, intermediate between that of $Ga_{0.47}In_{0.53}As$ and InP. In the limit of layer thicknesses of the order of a few monolayers the energy band gap can be approximated by the expression

$$E_g = \frac{E_g(Ga_{0.47}In_{0.53}As)L(Ga_{0.47}In_{0.53}As) + E_g(InP)L(InP)}{L(Ga_{0.47}In_{0.53}As) + L(InP)}, \qquad 10.$$

where the L's are the layer thicknesses.

These superlattices can be regarded as novel pseudo-quaternary GaInAsP semiconductors. In fact, like $Ga_{1-x}In_xAs_{1-y}P_y$ alloys, they are grown lattice-matched to InP and their band gap can be varied between that of InP and that of $Ga_{0.47}In_{0.53}As$. The latter is done by adjusting the ratio of the $Ga_{0.47}In_{0.53}As$ and InP layer thicknesses. Pseudo-quaternary GaInAsP is particularly suited to replace variable gap $Ga_{1-x}In_xAs_{1-y}P_y$. Such alloys are very difficult to grow since the mode fraction x (or y) must be continuously varied while maintaining lattice matching to InP.

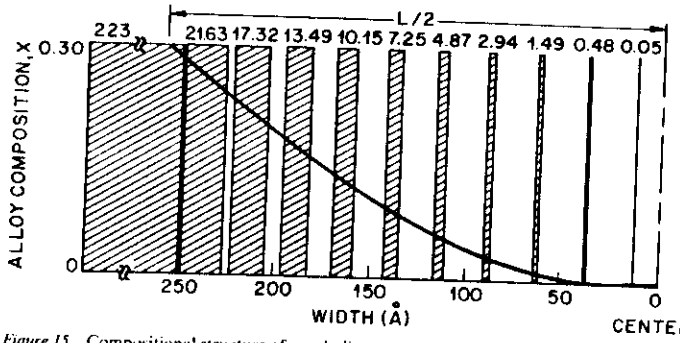

Figure 15 Compositional structure of parabolic quantum well versus distance from the well center (only half of the well is shown). The parabolic compositional profile (solid line) is obtained by growing a superlattice of alternated $Al_{0.3}Ga_{0.70}As$ and GaAs layers (dashed and white regions respectively) of varying thicknesses. The numbers at the top of the figure are the thicknesses of the $Al_{0.3}Ga_{0.70}As$ layers. (Courtesy of R. C. Miller.)

Figure 16*a* shows a schematic of the energy-band diagram of undoped (nominally intrinsic) graded-gap pseudo-quaternary GaInAsP. The structure consisted of alternated ultrathin layers of InP and $Ga_{0.47}In_{0.53}As$ and was grown by a new vapor phase epitaxial growth technique, levitation epitaxy (36). Other techniques, such as molecular beam epitaxy or metallorganic chemical vapor deposition, may also be suitable to grow such superlattices. From Figure 16*a* it is clear that the duty factor of the InP and $Ga_{0.47}In_{0.53}As$ layer is gradually varied, while the period of the superlattice is kept constant. As a result the average composition and band gap (dashed lines in Figure 16*a*) of the material are also spatially graded between the two extreme points (InP and $Ga_{0.47}In_{0.53}As$). In our structure both ten and twenty periods (1 period = 60 Å) were used. The InP layer thickness was decreased linearly with distance, from ≅50 Å to ≅5 Å,

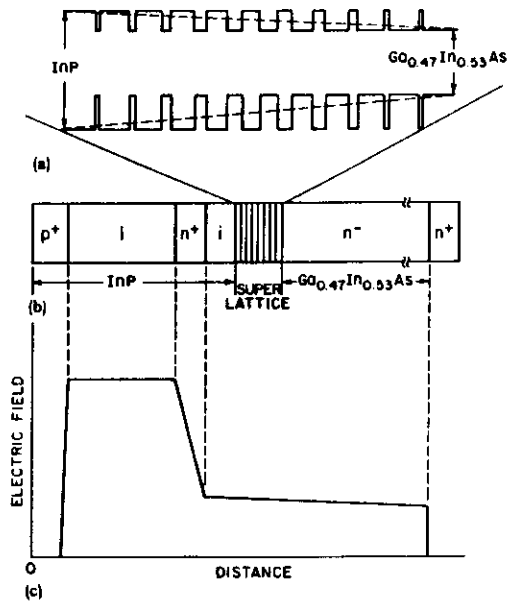

Figure 16 (*a*) Band diagram of a pseudo-quaternary graded-gap semiconductor. The dashed lines represent the average band gap seen by the carriers; (*b*) and (*c*) are the schematic structure and the electric field profile of a high-low avalanche photodiode using the pseudo-quaternary layer to achieve high speed. (From Reference 35.)

while the corresponding $Ga_{0.47}In_{0.53}As$ thickness was increased to keep the superlattice period constant (= 60 Å).

The graded-gap superlattice was incorporated in a long-wavelength $InP/Ga_{0.47}In_{0.53}As$ avalanche photodiode, as shown in Figure 16*b*. This device is basically a photodetector with separate absorption ($Ga_{0.47}In_{0.53}As$) and multiplication (InP) layers and a high-low electric field profile (HI-LO SAM APD). This profile (Figure 16*c*) is achieved by a thin doping spike in the ultralow doped InP layer and considerably improves the device performance compared to conventional SAM APD's (37). The $Ga_{0.47}In_{0.53}As$ absorption layer is undoped ($n \approx 1 \times 10^{15}$ cm^{-3}) and 2.5 μm thick. The n^+ doping spike thickness and carrier concentration were varied between 500 and 200 Å and 1×10^{17} to 5×10^{17} cm^{-3}, respectively (depending on the wafer), while maintaining the same carrier sheet density ($\cong 2.5 \times 10^{12}$ cm^{-2}). The n^+ spike was separated from the superlattice by an undoped 700 to 1000-Å-thick InP spacer layer. The p^+ region was defined by Zn diffusion in the 3-μm-thick low carrier density ($n \approx 10^{14}$ cm^{-3}) InP layer. The junction depth was varied from 0.8 to 2.5 μm. Similar devices without the superlattice region were also grown.

Previous pulse response studies of conventional SAM APD's with abrupt $InP/Ga_{0.47}In_{0.53}As$ heterojunctions found a long (>10 ns) tail in the fall time of the detector due to the piling up of holes at the heterointerface (38). This is caused by the large valence band discontinuity (≅0.45 eV). It has been proposed that this problem can be eliminated by inserting between the InP and $Ga_{0.47}In_{0.53}As$ region a $Ga_{1-x}In_xAs_{1-y}P_y$ layer of intermediate band gap (39). This quaternary layer is replaced in our structure by the $InP/Ga_{0.47}In_{0.53}As$ variable gap superlattice. This not only offers the advantage of avoiding the growth of the critical, independently lattice-matched GaInAsP quaternary layer, but also may lead to an optimum "smoothing out" of the valence band barrier for reproducible high-speed operation. This feature is essential for HI-LO SAM APD's since the heterointerface electric field is lower than in conventional SAM devices.

For the HI-LO SAM APD pulse response measurement we used a 1.55-μm GaInAsP device driven by a pulse pattern generator. Figure 17 shows the response to a 2-ns laser pulse with (*a*) and without (*b*) a 1300-Å-thick superlattice. Both devices had similar doping profiles and breakdown voltage (≅80 V) and were biased at −65.5 V. At this voltage the ternary layer was completely depleted in both devices, and the measured external quantum efficiency was about 70%. The results of Figure 17 were reproduced in many devices on several wafers. The long tail in Figure 17*b* is due to the pile-up effect of holes, which is associated with the abruptness of the heterointerface. In devices with the graded-gap superlattice (Figure 17*a*) there are no long tails. In these cases the height

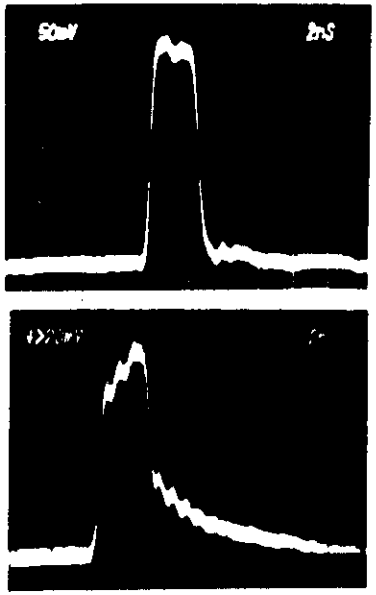

Figure 17 Pulse response of a high-low avalanche detector with pseudo-quaternary layer (*top*), and without (*bottom*), to a 2-ns, $\lambda = 1.55\ \mu m$ laser pulse. The bias voltage is -65.5 V for both devices; the time scale is 2 ns/div. (From Reference 35.)

of the barrier seen by the holes is no longer the valence band discontinuity ΔE_v, but

$$\Delta E = \Delta E_v - e\varepsilon_1 L, \qquad 11.$$

where ε_1 is the value of the electric field at the InP-superlattice interface and L is the thickness of the pseudo-quaternary layer. The devices are biased at voltage such that $\varepsilon_1 > \Delta E_v/eL$ so that $\Delta E = 0$ and no trapping occurs. In the devices with no superlattice instead ΔE is equal to ΔE_v for every ε_1, so long tails in the pulse response are observed at all voltages.

Conclusions

The previous discussion has illustrated the tremendous flexibility introduced by graded-gap material in heterostructure design. Band gap grading allows one to literally design and tailor the important transport properties to a given application (1). The most important characteristic of this band gap engineering approach is that the electron and hole transport properties

can be varied independently. Another characteristic is that the energy band diagram and the associated transport properties can be varied continuously. Thus the band gap can be considered, just as the doping or the layer thicknesses, as an independent design variable.

ACKNOWLEDGMENTS

It is a pleasure to acknowledge the many colleagues who have collaborated with the author: A. Y. Cho, A. C. Gossard, W. T. Tsang, H. M. Cox, R. J. Malik, B. F. Levine, J. A. Cooper, K. K. Thornber, S. Luryi, G. F. Williams, C. G. Bethea, A. L. Hutchinson, and R. A. Kiehl. R. C. Miller kindly supplied Figure 15. I am also grateful to J. A. Hutchby for enlightening discussions.

Literature Cited

1. Capasso, F. 1983. *J. Vac. Sci. Technol. B* 1: 457–61
2. Cho, A. Y., Arthur, J. R. 1975. *Progr. Solid State Chem.* 10: 157
3. Kroemer, H. 1957. *RCA Rev.* 18: 332
4. Miller, R. C., Kleinman, D. A., Gossard, A. C., Munteanu, O. 1984. *Phys. Rev. B* 29: 7085
5. Hutchby, J. A. 1978. *J. Appl. Phys.* 49: 4041–46
6. Levine, B. F., Tsang, W. T., Bethea, C. G., Capasso, F. 1982. *Appl. Phys. Lett.* 41: 470–72
7. Levine, B. F., Bethea, C. G., Tsang, W. T., Capasso, F., Thornber, K. K., et al. 1983. *Appl. Phys. Lett.* 42: 769–71
8. Capasso, F., Tsang, W. T., Bethea, C. G., Hutchinson, A. L., Levine, B. F. 1983. *Appl. Phys. Lett.* 42: 93–95
9. Kroemer, H. 1983. *J. Vac. Sci. Technol. B* 1: 126–29
10. Hayes, J. R., Capasso, F., Gossard, A. C., Malik, R. J., Wiegmann, W. 1983. *Electron. Lett.* 19: 410–11
11. Miller, D. L., Asbeck, P. M., Anderson, R. J., Eisen, F. H. 1983. *Electron. Lett.* 19: 367–68
12. Malik, R. J., Capasso, F., Stall, R. A., Kiehl, R. A., Wunder, R., Bethea, C. G. 1985. *Appl. Phys. Lett.* 46: 600–2
13. Malik, R. J., Hayes, J. R., Capasso, F., Alavi, K., Cho, A. Y. 1983. *IEEE Electron. Devices Lett.* 4: 383–85
14. People, R., Wecht, K. W., Alavi, K., Cho, A. Y. 1983. *Appl. Phys. Lett.* 43: 118–20
15. Hayes, J. R., Capasso, F., Malik, R. J., Gossard, A. C., Wiegmann, W. 1983. *Appl. Phys. Lett.* 43: 949–51
16. Tsang, W. T. 1981. *Appl. Phys. Lett.* 39: 134–37
17. Holonyak, N. Jr., Kolbas, R. M., Dupuis, R. D., Dapkus, P. D. 1980. *IEEE J. Quantum Electron.* 16: 134–37
18. Kazarinov, R. F., Tsarenkov, G. V. 1976. *Sov. Phys. Semicond.* 10: 178–82
19. Woodall, J. M., Hovel, H. J. 1977. *Appl. Phys. Lett.* 30: 492–93
20. Capasso, F., Tsang, W. T., Hutchinson, A. L., Foy, P. W. 1982. *Proc. 1981 Symp. GaAs and Related Compounds, Oiso*, Inst. Phys. Conf. Ser. 63, pp. 473–78. London: Inst. Phys.
21. McIntyre, R. J. 1966. *IEEE Trans. Electron. Devices* 13: 164–68
22. Price, P. J. 1981. *IEEE Trans. Electron. Devices* 28: 911–14
23. Allyn, C. L., Gossard, A. C., Wiegmann, W. 1980. *Appl. Phys. Lett.* 36: 373–76
24. Gossard, A. C., Brown, W., Allyn, C. L., Wiegmann, W. 1982. *J. Vac. Sci. Technol.* 20: 694–700
25. Capasso, F., Luryi, S., Tsang, W. T., Bethea, C. G., Levine, B. F. 1983. *Phys. Rev. Lett.* 51: 2318–21
26. Capasso, F., Williams, G. F., Tsang, W. T. 1982. *Tech. Digest IEEE Specialist Conf. on Light Emitting Diodes and Photodetectors, Ottawa*, Hull, pp. 166–67
27. Capasso, F., Tsang, W. T. 1982. *Tech. Digest Intern. Electron. Devices Meet., Washington, D.C.*, pp. 334–37
28. Capasso, F. 1983. *IEEE Trans. Nucl. Sci.* 30: 424–28
29. Capasso, F. 1983. *Surf. Sci.* 132: 527–39
30. Capasso, F., Tsang, W. T., Williams, G.

F. 1983. *IEEE Trans. Electron. Devices* 30: 381–90
31. Cooper, J. A. Jr., Capasso, F., Thornber, K. K. 1982. *IEEE Electron. Devices Lett.* 3: 402–8
32. Capasso, F., Tsang, W. T., Hutchinson, A. L., Williams, G. F. 1982. *Appl. Phys. Lett.* 40: 38–40
33. Kawabe, M., Matsuuza, N., Inuzuka, H. 1982. *Jpn J. Appl. Phys.* 21: L447–48
34. Miller, R. C., Kleinman, D. A., Gossard, A. C. 1984. *Phys. Rev. B* 29: 7085
35. Capasso, F., Cox, H. M., Hutchinson, A. L., Olsson, N. A., Hummel, S. G. 1984. *Appl. Phys. Lett.* 45: 1193–95
36. Cox, H. M. 1984. *J. Cryst. Growth* 69: 641–42
37. Capasso, F., Cho, A. Y., Foy, P. W. 1984. *Electron. Lett.* 20: 635–37
38. Forrest, S. R., Kim, O. K., Smith, R. G. 1982. *Appl. Phys. Lett.* 41: 95–97
39. Campbell, J., Dentai, A. G., Holden, W. S., Kasper, B. L. 1983. *Electron. Lett.* 19: 818–20

Quantum Functional Devices: Resonant-Tunneling Transistors, Circuits with Reduced Complexity, and Multiple-Valued Logic

EDERICO CAPASSO, FELLOW, IEEE, SUSANTA SEN, MEMBER, IEEE, FABIO BELTRAM, MEMBER, IEEE, EDA M. LUNARDI, MEMBER, IEEE, ARVIND S. VENGURLEKAR, MEMBER, IEEE, PETER R. SMITH, NITIN J. SHAH, MEMBER, IEEE, ROGER J. MALIK, MEMBER, IEEE, AND ALFRED Y. CHO, FELLOW, IEEE

(Invited Paper)

Abstract—Recent advances in the area of quantum functional devices are discussed. After a discussion of the functional device concept the introduction, in the second section resonant-tunneling bipolar nsistors (RTBT) with a double barrier in the base region are described. Design considerations for RTBT's with ballistic injection and first observation of minority-electron ballistic RT are presented. BT's using thermionic injection and exhibiting high peak-to-valley llo at room temperature in the transfer characteristics are also described. Multiple-state RTBT's and their dc and microwave performance are discussed in the third section. Circuit applications of RTBT's discussed in the fourth section. It is shown that RTBT's allow the plementation of many analog and digital circuit functions with a atly reduced number of transistors and show considerable promise multiple-valued logic. Experimental results on frequency multipliers and parity bit generators are presented. Analog-to-digital converters and memory circuits are also discussed. The structures presented in the last section are of interest primarily as tools to investigate physics of transport in superlattices and in two-dimensional systems. Two new superlattice base transistors are reported; negative nsconductance is achieved by suppression of injection into minibands. Gated quantum-well RT transistors are also discussed.

I. Introduction: Functional Devices

N a remarkable and pioneering paper [1] entitled "From Physics to Function," J. A. Morton of Bell Laboratories, more than 20 years ago, introduced the functional evice concept. The key characteristic of such devices is iat "they promise to reduce greatly the number of elements and process steps per function when their capabilies are properly matched to an old or new system function." Morton provided a few examples of functional evices, including the tunnel diode [2]. The charge-coupled device (CCD) [3], invented and developed in the 970's, is another early example of a functional device nce it can perform a wide range of electronic functions ncluding image sensing and signal processing.

There is no question that Morton was ahead of his time. His vision, strongly relying on dramatic progress in growth techniques, material science, and semiconductor physics, is only now gradually starting to become a reality. In particular the advent of advanced epitaxial growth techniques such as molecular-beam epitaxy (MBE) and metalorganic chemical vapor deposition (MOCVD) and of bandgap engineering [4] has made possible the development of a new class of materials and heterojunction devices with unique optical and electronic properties. The investigation of novel phenomena arising when the layer thicknesses become comparable to the de Broglie wavelength of electrons (quantum size effect) has proceeded in parallel with their exploitation in novel devices such as quantum-well (QW) lasers, invented in the 1970's.

The invention of functional devices (in the sense of Morton) based on quantum confinement, however, occurred later in the early 1980's. In the optoelectronics area an excellent example is the self-electrooptic effect device (SEED) [5], based on the quantum confined Stark effect, which may have an important impact on photonic switching. Resonant-tunneling (RT) transistors are emerging instead as some of the most promising electron functional devices.

RT through heterojunction double barriers (DB's) was first observed by Chang *et al.*, in 1974 [6]. However, the observed negative differential resistance (NDR) effects were too small to be useful in device applications. The impressive RT experiments at terahertz frequencies of Sollner *et al.* in 1983 [7] stimulated renewed interest in NDR. Oscillation frequencies in excess of 400 GHz have been demonstrated [8]. The remarkable progress in MBE during the last decade has recently made possible the observation of high peak-to-valley ratios in RT DB's [9]. The literature on RT DB's is vast. The interested reader is referred to recent reviews [10], [11] covering the physics as well as the dc and high-frequency performance of RT diodes.

As early as 1963, Davis, Hosack, and Iogansen suggested that the well in a unipolar RT DB could act as the control electrode of a transistor [12], [13].

Manuscript received March 13, 1989; revised June 23, 1989.
The authors are with AT&T Bell Laboratories, Murray Hill, NJ 07974.
IEEE Log Number 8930567.

In 1984, Capasso and Kiehl proposed the concept of a resonant-tunneling bipolar transistor (RTBT) [14]. Independently, Riccò and Solomon [15] discussed a similar device. RT transistors allow the implementation of a large class of circuits (e.g., analog-to-digital converters, parity checkers, frequency multipliers, etc.) with greatly reduced complexity (i.e., less transistor per function compared to a circuit using conventional transistors) [14]. The inherent functionality of these and other quantum electron devices has led a group at Texas Instruments to project an intriguing scenario for the future of electronics [16]. The progress of integrated circuits has so far been marked by increased levels of miniaturization to the point that nowadays certain VLSI chips contain an average of 10^7 components. Due to interconnection limitations, this scaling strategy will probably approach practical limits at a minimum lateral dimension of patterned geometries of $\sim 0.25\ \mu$m [16]. After reaching the limits of conventional scaling some time in the next 20 years, electronics will have to find new paths for its evolution in order to survive as an industry. New devices and circuit architectures will be devised. RT transistors and quantum-coupled devices may provide a way out, in light of their functionality and the possibility of direct device interconnections via tunneling [16]. It has also been pointed out that the inherent multistate nature of RT transistors could lead to new computer architectures using multiple-valued logic [14].

In 1985, Yokohama *et al.* [17] at Fujitsu reported the low-temperature (77 K) operation of a resonant-tunneling hot-electron unipolar transistor (RHET). (For a comprehensive review of RHET's, see [18].) Room-temperature operation of a RTBT, with a DB in the base, was demonstrated in 1986 by Capasso *et al.* at Bell Labs [19]. An RTBT with a single DB in the emitter was reported by Futatsugi *et al.* [20] at about the same time.

The emergence of AlInAs/GaInAs as a heterojunction ideally suited for RT devices, due to the light electron mass in the barrier (AlInAs) and the relatively large (direct gap) conduction band discontinuity [21], has further increased the pace of progress in this area, with many groups currently involved in RT transistor research. Recently, the first multiple-state RT transistor was demonstrated, along with its circuit capabilities [22], [23].

This paper discusses recent advances made by our group at Bell Laboratories in the area of quantum-effect transistors and their circuit applications.

II. Resonant-Tunneling Bipolar Transistors (RTBT's) with Double Barrier in the Base

The concept of an RTBT originated with the general idea, conceived by Capasso and Kiehl in 1984, of associating to each state of a quantum system (for example, the energy levels of a quantum well) a corresponding logic level [14].

This general scheme leads naturally to the idea of multiple-valued logic. Although such logic has been the subject of considerable investigation [24], all circuits so far proposed and demonstrated employed two-state devices.

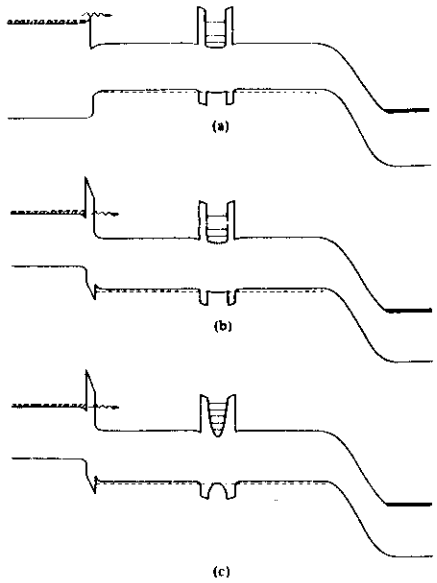

Fig. 1. Band diagram of resonant tunneling transistors with (a) abrupt and (b), (c) tunneling emitter.

The resulting architectures are therefore complex and cumbersome. The above correspondence (energy levels/logic states) led to the conception of a class of bipolar devices with inherent multistate operation [14].

Fig. 1 illustrates this type of device. It should be noted that although these transistors utilize nonequilibrium injection, the underlying operating principle is at the basis of the operation of all other RTBT's with the quantum well in the base irrespective of the details of the base contact. As the base-emitter voltage is increased, RT through each subband first reaches a maximum and is then quenched as the bottom of each QW subband is lowered below the conduction band edge in the emitter. This produces multiple peaks in the collector current, i.e., multiple negative transconductance. A tunnel emitter device with a parabolic well in the base can be used to generate equally spaced peaks. For example, using a well of width 200 Å with an $Al_{0.45}Ga_{0.55}As$ barrier, one finds an energy level separation ≈ 64 meV. This gives a total of five states in the well. In a recent experiment [25], as many as 16 resonances were observed in RT diodes with a parabolic well.

A. Design Considerations for RTBT's with Ballistic Injection

The design of the transistors of Fig. 1 is critical. This is due to various requirements that must simultaneously be satisfied in order to achieve acceptable current densities ($\gtrsim 10^4 A/cm^2$), current gains ($\gtrsim 10$), and peak-to-

valley ratios ($>2:1$). We assume first that the RT through the DB is coherent; this can be achieved by designing the DB so that $\hbar/\Gamma \ll \tau_\phi$, where Γ is the resonance full width at half maximum and τ_ϕ is the phase relaxation time [26]. An estimate of τ_ϕ can be obtained from the reciprocal of the *total* scattering rate $1/\tau_T$ (inelastic + elastic) at the energy of the incident particle [26]. As an example, in GaAs at a concentration $p = 5 \times 10^{18}$ cm^{-3}, $1/\tau_T$ is in the range from 2×10^{13} s^{-1} to 2.5×10^{13} s^{-1} for injection energies in the range from 0.1 to 0.3 eV [27]. Thus, to ensure that the above condition for coherent transport is satisfied, Γ should be larger than ~ 10 meV. This can be achieved with the ground state resonance ($E_1 = 133$ meV) of an $Al_{0.40}Ga_{0.60}As$ (15 Å)/GaAs (30 Å) DB, for which tunneling resonance calculations show $\Gamma \approx 64$ meV. The coherence of the RT process and the lateral momentum conservation during tunneling ensure that in symmetric DB's incident electrons with a perpendicular energy $E_\perp$ equal to the bottom of one of the subbands of the well traverse the DB with unity transmission. However, in any experimental situation the incident perpendicular energy distribution function (per unit volume and unit energy) $n_\perp(E_\perp)$ has a finite width ΔE; in order to exploit coherent RT and achieve a high base transport factor, ΔE must be smaller than Γ. If $\Delta E \gg \Gamma$ (a situation commonly encountered in DB diodes), only a small fraction of the incident electrons $\sim \Gamma/\Delta E$ contributes to the RT current J_R. J_R is then approximately given by

$$J_R = e v_R n_\perp(E_R)\, \Gamma T_R \qquad (1)$$

where $T_R \approx 1$, E_R is the transmission resonance energy, and v_R is the perpendicular component of the velocity corresponding to $E_\perp = E_R$. Since $\Gamma \approx E_R T_B$ where T_B is the transmission of the individual barriers (usually $\ll 1$), (1) shows that, for a broad incident distribution, it is the transmission of the individual barriers and not the overall transmission of the DB to determine the current [28]. Therefore, to maximize J_R, ΔE must be smaller than Γ. To achieve this, the energy distribution in the emitter should be narrower than the resonance width, and electrons should traverse the distance between the DB and the emitter quasi-ballistically. The width of the emitter energy distribution perpendicular to the barrier is approximately $k_B T + \Phi_n$, where $k_B T$ is the thermal energy and Φ_n is the quasi-Fermi energy in the emitter, which is comparable to the equilibrium Fermi level.

Consider first the structure of Fig. 1(a). The emitter composition should be chosen in order to have $\Delta E_c \approx E_1$ so that under resonance conditions the conduction band in the emitter is nearly flat to maximize the peak collector current. If ΔE_c is significantly smaller than E_R, then the base–emitter junction must be biased beyond flat band to achieve resonance. In this case, the electric field in the emitter will heat the injected distribution and broaden it, an unwanted effect in light of the above discussion. On the other hand, if ΔE_c is significantly larger than E_R, then at resonance the emitter current will not be large enough due to the residual base–emitter barrier. Consider, for example, the $Al_{0.4}Ga_{0.6}As$/GaAs DB previously discussed. The emitter composition should be chosen to be approximately $Al_{0.20}Ga_{0.60}As$, which corresponds to $\Delta E_c \approx E_1 = 133$ meV. For an emitter doping density of 5×10^{17} cm^{-3}, the width of the distribution ballistically launched with an energy $E_\perp = \Delta E_c$ by the abrupt emitter is ≈ 50 meV, which is close to the resonance width in the DB. One must, however, also consider the effects of scattering in the region between the DB and the emitter, which broadens the distribution. In order to achieve a high peak-to-valley ratio, scattering in this region must be minimized. Electrons are launched by the emitter with a forward velocity $(2\Delta E_c/m^*)^{1/2} \approx 8 \times 10^7$ cm/s limited by the band structure. Since the scattering rate at the injection energy is $\approx 2 \times 10^{13}$ s^{-1} (for $p = 5 \times 10^{18}$ cm^{-3} in the base), the mean free path for these electrons is $\lambda \approx 400$ Å [27]. If the distance between the DB and the emitter (L) is kept at ≈ 300 Å, this implies that only half of the carriers ($\approx \exp -L/\lambda$) traverse this distance without collisions. Electrons that have lost a portion ($\geq$ optical phonon energy, ≈ 35 meV, for the $Al_{0.4}Ga_{0.6}As$ (15 Å)/GaAs (30 Å) DB case under consideration) of their energy normal to the DB as a result of these collisions will see a significantly reduced transmission through the DB or "miss" the first resonance altogether if the width of the latter is too small.

One way to considerably reduce the scattering rate is to dope extremely heavily ($>10^{20}$ cm^{-3}) the region between the DB and the emitter. Recent theoretical work by Levi *et al.* [27] has shown that the inelastic scattering rate of minority-carrier electrons in p-type GaAs first increases with increasing doping and rapidly decreases for doping levels well above 10^{19} cm^{-3}, due to the decreased phase space available for scattering. These levels can be achieved by carbon doping [29], which also has the advantage of a small diffusion coefficient. At the same time, elastic scattering, which increases rapidly with increasing doping, can be strongly suppressed by placing impurities in a periodic sublattice by delta doping techniques [30]. Scattering rate calculations show that, at injection energies of ≈ 0.15 eV and for $p = 2 \times 10^{20}$ cm^{-3}, mean free paths as long as 1500 Å can then be achieved in GaAs [27]. In this way one can minimize scattering in the region between the DB and the emitter. These considerations of course also apply to the structures of Fig. 1(b) and (c).

The above discussion clearly demonstrates that the design of an RTBT with quasi-ballistic injection is an extremely difficult task. This may be somewhat easier to do in AlInAs/GaInAs and InP/GaInAs systems in light of the larger mean free path of electrons in p-type $Ga_{0.45}In_{0.53}As$ (approximately twice that of GaAs at the same injection energy) and the smaller effective masses in the barrier and well layers. The preferred structure in this case would have a tunnel emitter of the type shown in Fig. 1(b), (c) and consisting of a $Ga_{0.45}In_{0.53}As$ layer followed by an InP or an $Al_{0.48}In_{0.52}As$ tunnel barrier. Tunnel emitters allow one to bias the base–emitter junction well beyond flat band while still maintaining a narrow incident energy distribution.

B. Observation of Quasi-Ballistic Resonant Tunneling in a Tunneling Emitter RTBT

In this section we present results on the RTBT of Fig. 1(b), fabricated in the AlInAs/GaInAs system. The collector layer is 3000-Å-thick undoped $Ga_{0.47}In_{0.53}As$. The base layer comprises a 600-Å region on the emitter side (doped to $p = 3 \times 10^{18}$ cm^{-3}) and a 2000-Å region, doped to $p = 5 \times 10^{18}$ cm^{-3}, on the collector side, separated by an undoped $Al_{0.48}In_{0.53}As$ (50 Å)/$Ga_{0.47}In_{0.53}As$ (100 Å) DB. The emitter consists of an undoped $Al_{0.48}In_{0.52}As$ 30-Å tunnel barrier separated from the base by a 50-Å undoped space layer and followed by an $n = 1 \times 10^{18}$ cm^{-3} 3000-Å-thick $Ga_{0.47}In_{0.53}As$ layer.

The device transfer characteristic in the common-base configuration is shown in Fig. 2 at $V_{CB} = 1.0$ V at cryogenic temperature. The collector current rises rapidly above the built-in voltage ($V_{bi} = 0.8$ V) and peaks at ≈ 1.25 V. This value equals the calculated voltage required to line up the bottom of the first quantized subband in the accumulation layer on the emitter side of the tunnel barrier with the second resonance of the well ($E_2 = 193$ meV). Thus, this peak corresponds to the ballistic RT of electrons injected from the emitter in the first excited state of the QW.

Note that the negative transconductance region after the peak is broad (≈ 0.2 eV) and the peak-to-valley ratio is small. These features can be understood as follows. The mean free path in p^+-InGaAs for electrons with kinetic energies of the order of 100 meV can be estimated to be about 500 Å [31]. A large fraction of the electron distribution incident on the DB is therefore nonballistic due to scattering in the region between the emitter and the DB. The dominant scattering mechanisms for electrons in p^+-InGaAs doped to densities $>10^{18}$ cm^{-3} are inelastic collisions with holes and coupled phonon–plasmon modes [31]. Assume now that the emitter–base junction is biased beyond the second resonance of the quantum well (QW) so that the electron injection energies exceed E_2. The injected electrons that approach the DB ballistically have their energy mostly associated with perpendicular motion so that $E_\perp > E_2$. These electrons therefore cannot resonantly tunnel into the QW. On the other hand, the part of the electron distribution that evolves following scattering has electrons with reduced $E_\perp$. This part contains electrons with $E_\perp$ equal to E_1 and E_2 so that they are still able to resonantly tunnel into the QW when incident on the DB. This provides an increasing background to the collector current as V_{EB} increases. We therefore have a rather broad peak region and a small peak-to-valley ratio in Fig. 2. Since the DB region in our device has no intentional dopant impurities, the possible effects of elastic scattering centers in the QW on the peak-to-valley ratio [32] are relatively unimportant in the present case.

Previous work by some of us [33] on the RT spectroscopy of electrons injected via band discontinuities in p^+

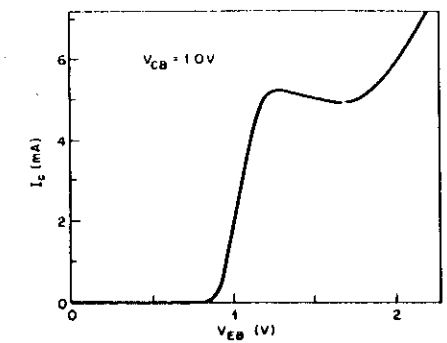

Fig. 2. Transfer characteristics of the resonant tunneling transistor of Fig 1(b) at 10 K.

GaAs wells observed the formation of a broad hot distribution induced by scattering, but failed to detect ballistic effects, probably due to the shorter electron mean free path in GaAs.

It is interesting to note that we have not observed a peak corresponding to the first resonance of the well ($E_1 = 41$ meV). This is primarily due to the fact that the peak current associated with the first resonance is smaller than the one through the resonance by the ratio (~ 10) of the transmission coefficients of the individual barrier at the two resonant energies (see (1)), so that the first peak is masked by the rapidly rising emitter current for $V_{EB} > V_{bi}$; in addition, the effects of scattering on the incident distribution will reduce the peak-to-valley ratio and broaden the peak, as previously discussed.

C. Thermionic Injection RTBT's Operating at Room Temperature

The first operating RTBT was demonstrated by Capasso *et al.* in 1986 [19] and was designed to have minority electrons thermally injected into the DB. This makes the design of the device much less critical; the structure implemented in the AlGaAs system operated at room temperature. The band diagram of this transistor is shown in Fig. 3(a), (b) under operating conditions. The alloy composition of the region adjacent to the emitter is adjusted in such a way that the conduction band in this region lines up with, or is slightly below, the bottom of the ground-state subband of the QW. For the 74-Å well with 21.5-Å AlAs barriers, the first quantized energy level is $E_1 = 65$ meV. Thus, the Al mole fraction was chosen to be $x = 0.07$ (corresponding to $E_g = 1.521$ eV) so that $\Delta E_c \approx E_1$. The QW is undoped; nevertheless, it is easy to show that there is a high concentration ($\approx 7 \times 10^{11}$ cm^{-2}) of two-dimensional hole gas in the well. These holes have transferred by tunneling from the nearby $Al_{0.07}Ga_{0.93}As$ region. This reduces scattering in the well by essentially eliminating elastic scattering by the doping impurities [32]. Electrical contact was made to both the well region and the GaAs portion of the base adjacent to the DB, but not to the $Al_{0.07}Ga_{0.93}As$ region. The wide

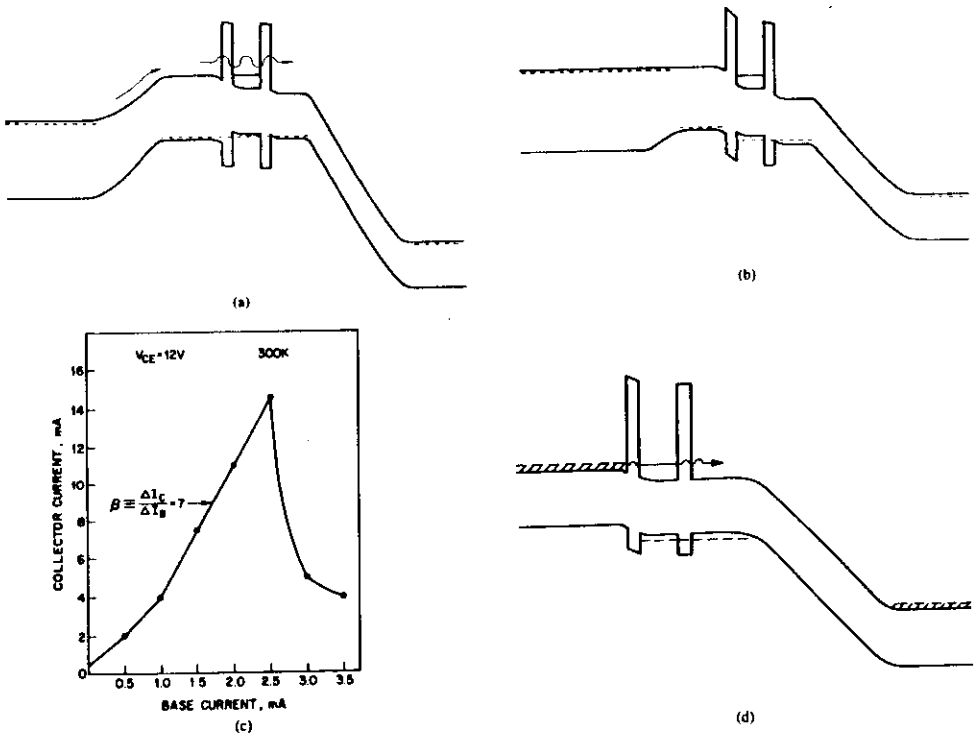

Fig. 3. Energy band diagrams of the RTBT with thermal injection for different base currents I_B at a fixed collector emitter voltage V_{CE} (not to scale). As I_B is increased, the device first behaves as a conventional bipolar transistor with current gain (a), until near flat-band conditions in the emitter are achieved. For $I_B > I_{BTH}$, a potential difference develops across the first AlAs barrier. This raises the conduction band edge in the emitter above the first resonance of the well, thus quenching resonant tunneling and the collector current (b). The collector current versus base current in the common emitter configuration, at room temperature, is shown in (c). The line connecting the data points is drawn only to guide the eye. An alternative RTBT design is shown in (d).

gap emitter ($Al_{0.25}Ga_{0.75}As$) provides the well known advantages of heterojunction bipolar transistors (HBT's). Details of the structure and of the processing are given in [19].

In order to understand the operation of the device, consider a common-emitter bias configuration (Fig. 3(a), (b)). Initially the collector-emitter voltage V_{CE} and the base current I_B are chosen in such a way that the base-emitter and the base-collector junctions are, respectively, forward and reversed biased. If V_{CE} is kept constant and the base current I_B is increased, the base-emitter potential also increases until a flat conduction band condition in the emitter-base junction region is reached. The device in this regime behaves as a conventional transistor with the collector current linearly increasing with the base current (Fig. 3(c)). The slope of this curve is, of course, the current gain β of the device. In this region of operation, electrons in the emitter overcome, by thermionic injection, the barrier of the base-emitter junction and undergo RT through the DB. If the base current is further increased above the value I_{Bth} corresponding to the flat-band condition, the additional potential difference drops primarily across the first semi-insulating AlAs barrier (Fig. 3(b)) since the highly doped emitter is now fully conducting. This pushes the conduction band edge in the $Al_{0.07}Ga_{0.93}As$ above the first energy level of the well, thus quenching the RT. The net effect is that the base transport factor and the current gain are greatly reduced. This causes an abrupt drop of the collector current as the base current exceeds the threshold value I_{Bth} (Fig. 3(c)). Thus, the device has negative transconductance.

It should be clear that this device is not equivalent to a series combination of an RT diode and a bipolar transistor since electrical contact is made to the QW. Thus, the base-emitter voltage directly modulates the energy difference between the states of the well and the emitter quasi-Fermi level (see Fig. 3). Recently an RTBT based on this operating principle but with the base layer restricted to the GaAs quantum well was reported [34], as originally proposed by Riccò and Solomon [15].

Yokoyama *et al.* [18] reported an RTBT with the DB between the base and the emitter, exhibiting negative transconductance at liquid-nitrogen temperature. Since the quantum well is not contacted and is placed out of the base, this device, unlike the ones of [19] and [34], can be thought of as a monolithic series integration of a DB and a bipolar transistor.

Several alternative RTBT designs are possible; one is shown in Fig. 3(d). Here the p-region between the DB and the emitter is eliminated. The well is heavily doped with low-diffusion acceptors (e.g., C). The operating principle is the same as that of the device of Fig. 3(a), (b).

D. Speed and Threshold Uniformity Considerations in RTBT's

The insertion of a DB in an HBT structure offers new interesting circuit opportunities but also raises questions concerning its effects on speed and threshold uniformity.

With regard to the speed issue, the introduction of a DB in the base or in the emitter will increase the emitter-collector delay time τ_{ec} and therefore reduce the cutoff frequency f_T. This is due to the tunneling delay time, which in general is a complicated function of the shape of the incident perpendicular energy distribution. If the latter is much broader than the resonance width and nearly centered on one of the resonances, it can be shown that τ_T is approximately given by [10]

$$\tau_T = \frac{d}{v_G} + \frac{2\hbar}{\Gamma}. \tag{2}$$

The first term represents the semiclassical transit time across the RT structure of width d and is $\lesssim 0.1$ ps for the RTDB's of interest here. The second term is the so-called phase time. In the RT transistor structures with potential practical impact (e.g., Fig. 3), the first resonance width is much smaller than the quasi-Fermi energy in the emitter, thus satisfying the first assumption underlying (2). The condition that the tunneling wave function be nearly centered on the resonance is only partially valid, thus making (2) good for an approximate estimate of the delay time associated with RT. It is clear from this expression that to minimize τ_T, the resonant width Γ_1, which depends exponentially on the barrier thickness, must be maximized.

Consider an RTBT structure of the type previously discussed (Fig. 3). For a 17-Å AlAs barrier thickness and a 45-Å GaAs well, tunneling resonance calculations give $E_1 = 0.136$ eV for the first energy level and $2\hbar/\Gamma_1 = 0.45$ ps [10]. The first term in (2) is 0.08 ps (assuming a drift velocity $\geq 10^7$ cm/s since overshoot effects following injection in the DB are possible [10]). Thus, $\tau_T \approx 0.5$ ps. It is well known that AlGaAs/GaAs HBT's without an RTDB and uniform composition in the base can achieve f_T's > 50 GHz. The introduction of the above DB in an HBT with $f_t = 50$ GHz will increase τ_{ec} by 0.5 ps thus giving $f_T \approx 43$ GHz. This example shows that RTBT's with suitably designed DB's should have cutoff frequencies and overall speed of response comparable to that of state-of-the-art HBT's. A $Ga_{0.47}In_{0.53}As$ HBT with an $Al_{0.48}In_{0.52}As$ (44 Å)/$Ga_{0.47}In_{0.53}As$ (38 Å) DB in the emitter having an f_T of 12.5 GHz has recently been reported (see [18]). The microwave performance of multistate RTBT's will be reported in the next section.

Concerning the threshold (V_{BTH}) uniformity issue, let us recall that a conventional HBT has excellent uniformity (approximately a few millivolts) both on the same wafer and from wafer to wafer since V_{BTH} is given by the base-emitter built-in voltage. The latter is proportional to the bandgap and weakly (logarithmically) dependent on doping. The introduction of a DB in an HBT will induce greater fluctuations in V_{BTH}. To estimate the latter, consider the case of an RTBT with a DB in either the emitter or the base. The voltage position of the collector current peak (transistor fully on) is approximately given by $V_{BE} + 2E_1/e$ where E_1 is the energy of the first resonance of the well. E_1 can fluctuate across a wafer primarily due to in plane thickness fluctuations Δl. Assuming for E_1 the well known formula of an infinite potential well (this assumption provides an upper limit for the fluctuations in E_1), one finds that $\Delta E_1 = 2E_1 \Delta l/l$. Thus, the corresponding fluctuation in the peak position is

$$\Delta V_p = \Delta V_{BE} + \frac{4E_1}{e}\frac{\Delta l}{l}. \tag{3}$$

Thickness fluctuations in state-of-the-art MBE material are of the order of one monolayer, i.e. $\Delta l = 2.83$ Å. For an RTBT with the double barrier considered in this section, (3) therefore gives $\Delta V_p = 34$ mV. One obtains $\Delta V_p = 21.5$ mV for an RTBT containing an AlInAs (25 Å)/GaInAs (50 Å) DB. Values $\lesssim 100$ mV are adequate for the circuits envisioned with this technology.

III. Devices with Multiple Peak *I-V* Characteristics and Multiple-State RTBT's

A simple approach to realize multiple-peak *I-V* characteristics is the integration of a number of RT diodes. In this method, a single resonance of different quantum wells is used to generate the multiple peaks. Hence, they occur at almost the same current level and exhibit similar peak-to-valley ratios as required by the circuit applications that will be discussed in the following. However, these devices do not have the gain and input-output isolation of three-terminal devices.

There are two different ways to integrate RT diodes to achieve this characteristic. One is to horizontally integrate them [35], [36] so that the diodes are in parallel in the equivalent circuit. The other is to vertically integrate them [37], [38] so that they are in series. In this section we shall discuss only the latter approach since it is important for the design of the multistate RTBT. The rest of the section is devoted to RTBT's with multiple peaks in the transfer characteristics and their digital and analog circuit applications.

A. Vertical Integration of RT Diodes

Vertical integration of RT structures is achieved by stacking a number of DB's in series, separated by heavily doped cladding layers to quantum mechanically decouple the adjacent DB's from each other [37], [38]. The DB's are designed so that the ground state in the QW is substantially above the Fermi level in the adjacent cladding layers. The band diagram of the structure under bias is shown in Fig. 4. When bias is applied, the electric field is higher at the anode end of the device (Fig. 4(a)) because of the charge accumulated in the QW's under bias. Quenching of RT is thus initiated across the DB adjacent to the anode and then sequentially propagates to the other end as the high-field region widens with increasing applied voltage, as shown in Fig. 4(a) and (b). Once RT has been suppressed across a DB, the voltage drop across it quickly increases with bias because of the increased resistance. The non-RT component through this DB provides continuity for the RT current through the other DB's on the cathode side. An NDR region is obtained in the I–V, corresponding to the quenching of RT through each DB. Thus, with n diodes, n peaks are present in the I–V.

Generating multiple peaks by combining tunnel diodes in series is well known [39]. However, the mechanism in that arrangement is different. The tunnel diodes used in such a combination must have different characteristics with successively increasing peak currents, so that each of them can go into the NDR region only when the corresponding current level is reached [39]. Besides structures using RT, diodes have significant advantages over ones using tunnel diodes [35].

We have tested devices consisting of two, three and five $Al_{0.48}In_{0.52}As$ (50 Å)/$Ga_{0.47}In_{0.53}As$ (50 Å) DB's in series, separated by a 1000-Å-thick n^+ $Ga_{0.47}In_{0.53}As$ region. The resulting I–V characteristics taken in both polarities of the applied voltage at room temperature are shown in Fig. 5(a), (b), and (c). Positive polarity here refers to the top of the mesa being biased positively with respect to the bottom. Note that in this polarity, the devices show two, three, and five peaks in the I–V characteristics as expected. In the negative polarity, the third peak is not observed in the device with three DB's because of rapidly increasing background current. This is believed to be due to structural asymmetry unintentionally introduced during growth.

B. Multi-State RTBT's

The stacked RT structure discussed above was used to design an RTBT exhibiting multiple NDR and negative transconductance characteristics [22], [23]. A schematic of this transistor is shown in Fig. 6. The device essentially consists of a $Ga_{0.47}In_{0.53}As/Al_{0.48}In_{0.52}As$ n-p-n transistor with a stack of two $Ga_{0.47}In_{0.53}As$ (50 Å)/$Al_{0.48}In_{0.52}As$(50 Å) RT DB's, as discussed before, embedded in the emitter. Details of the structure (doping and layer thicknesses) are described in [22].

The operation of the transistor can be understood from the band diagrams in the common-emitter configuration

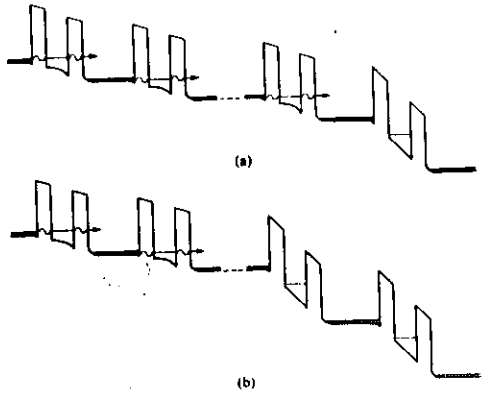

Fig. 4. Vertical integration of resonant tunneling diodes. Band diagram under applied bias (a) with RT quenched through the DB adjacent to the anode and (b) after expansion of the high-field region to the adjacent DB with increasing bias. The arrows indicate the RT component of the current.

Fig. 5. Current-voltage characteristics of the devices with (a) two, (b) three, and (c) five vertically integrated RT double barriers, taken for both bias polarities at 300 K.

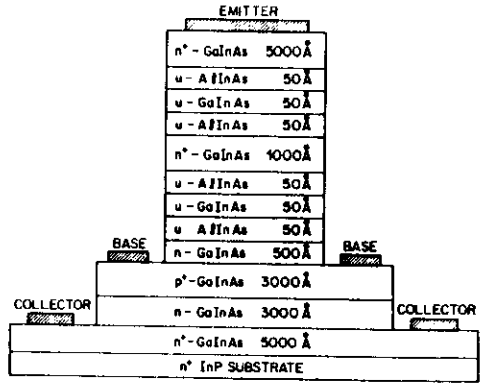

Fig. 6. Schematic structure of the multiple-state RTBT.

shown in Fig. 7. The collector-emitter bias (V_{CE}) is kept fixed and the base-emitter voltage (V_{BE}) is increased. For V_{BE} smaller than the built-in voltage ($V_{Bi} \simeq 0.7$ eV at 300 K) of the $Ga_{0.47}In_{0.53}As$ p-n junction, most of the bias voltage falls across this junction (Fig. 7(a)), since its impedance is much greater than that of the two DB's in series, both of which are conducting via RT. The device in this region behaves as a conventional bipolar transistor with the emitter and hence the collector current increasing with V_{BE} (Fig. 8) until the base-emitter junction reaches the flat-band condition. Beyond flat band, most of the additional increase in V_{BE} will fall across the DB's (Fig. 7(b)), and as RT through these quenches sequentially by the mechanism of Fig. 4, abrupt drops in the emitter and hence the collector current are observed (Fig. 8). The highest peak-to-valley ratio in the transfer characteristics at room temperature is 4:1 while it increases to about 20:1 at 77 K.

Fig. 9 shows the common-emitter output characteristics of the transistor (I_C versus V_{CE} at different I_B) at room temperature and 77 K. At low base currents I_B (and hence low base-emitter voltages V_{BE}), the device behaves as a conventional bipolar transistor as discussed before, with a large differential current gain (200 at 77 K and 100 at 300 K). With increasing I_B (V_{BE}) beyond the flat-band condition, the excess applied voltage V_{BE} starts appearing across the series of DB's in the emitter; as RT through them quenches sequentially, at threshold base currents I_{Bth1} and I_{Bth2}, the electron current across the base-emitter junction drops abruptly. This results in sudden quenching of the current gain at these threshold base currents and hence the collector current I_C also quenches, giving rise to two NDR regions (Fig. 9). The highest peak-to-valley ratio observed is 6:1 at room temperature and 22:1 at 77 K. It should be noted that the small-signal current gain of the transistor at room temperature in its second (1.2 mA $< I_B <$ 1.6 mA) and third ($I_B >$ 1.6 mA) operation regions is reduced to 40 and 20, respectively. This is expected since the hole current flowing from the base toward the emitter increases with increasing V_{BE}, thus reducin the injection efficiency. This reduction of the current ga is less pronounced at 77 K, since the thermionic flow c holes is much lower at that temperature.

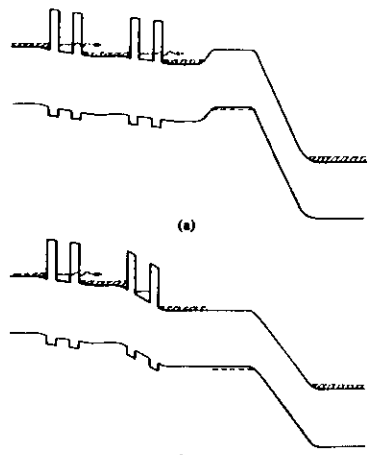

Fig. 7. Band diagram of the multiple-state RTBT in the common emitt configuration for different base-emitter bias conditions. (a) Electro resonantly tunnel through both DB's; in the regime, the transistor ope ates as a conventional bipolar. (b) Quenching of RT through the D adjacent to the p-n junction gives rise to a negative transconductan region in the collector current. Quenching of RT through the other D produces a second peak in the I–V.

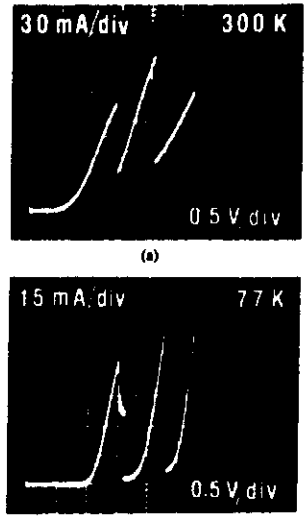

Fig. 8. Collector current versus base-emitter voltage, in the comm emitter configuration for $V_{CE} = -0.1$ V at (a) 300 K and (b) 77 K.

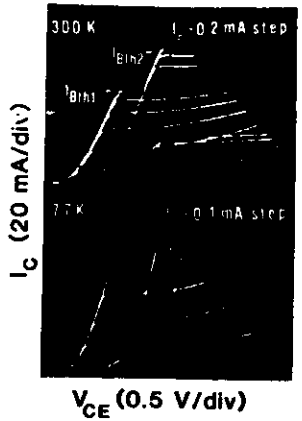

Fig. 9. Common emitter output characteristics of the multiple-state RTBT. Collector current versus collector-emitter voltage for different base currents, at (a) 300 K and (b) 77 K.

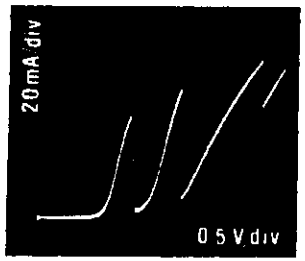

Fig. 10. Common-emitter transfer characteristics of a multiple-state RTBT with three DB's in the emitter at 77 K. I_C versus V_{BE} is shown for V_{CE} = 4.75 V.

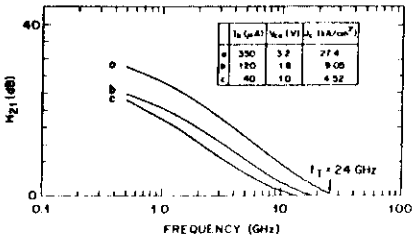

Fig. 11. Current gain (h_{21}) as a function of frequency for different bias points in the common-emitter configuration. Also indicated is the corresponding collector current density J_c.

Fig. 10 shows the common-emitter transfer characteristics of a similar transistor with three DB's in the emitter at 77 K. The third peak is shifted out to a significantly higher voltage compared to the other two. Our systematic studies also indicated large hysteresis associated with the same. Such behavior is not uncommon in RT devices whenever there is large parasitic resistance [40]. When three DB's are put in series, the parasitics also add up and enhance the effect. The structure with three peaks has to be optimized to minimize these effects.

To minimize the flow of holes from the base to the emitter, an n^+ $Al_{0.48}In_{0.52}As$ layer can be inserted between the stack of DB's and the base, similar to the use of a wide-gap emitter in HBT's. Preliminary results with an $n = 1 \times 10^{18}$ cm^{-3} 500-Å AlInAs layer, followed by the growth of an equally thick and doped AlInGaAs grading layer before the DB's, give a β of 4000 at 77 K.

C. Microwave Performance of Multistate RTBT's

In this section, we report the high-frequency operation of RTBT's [41].

The device structure, grown lattice matched to an InP substrate by MBE, is very similar to the one previously discussed in Section III-B. For microwave evaluation, the present structure was grown on a semi-insulating InP substrate instead of an n^+ one. Furthermore, the base-layer thickness was reduced by a factor of two, down to 1500 Å, and the doping was doubled (4×10^{18} cm^{-3}) to reduce the base transit time without increasing the base resistance.

The emitter-up transistor in a mesa configuration was obtained by successive steps of photolithography and wet chemical etching to expose the base and collector layers. After planarization of the structures with dielectric deposition, a nonalloyed metallization (Ti/Au) was deposited for the contacts. The emitter area is 42 μm^2. The *I-V* characteristics of the devices are virtually identical to those of Figs. 8 and 9. The only difference is that the collector currents are considerably smaller due to the scaled down area.

Scattering (S) parameter measurements were performed in the frequency range from 0.5 to 26.5 GHz using a wafer prober in conjunction with an automatic network analyzer (HP8510B). Fig. 11 displays the current gain (h_{21}) as a function of frequency for different bias conditions. Curve (*a*) refers to an operating point after the second peak in the common-emitter characteristics. The f_T obtained by extrapolation using a −20-dB/decade straight line is 24 GHz, which is the highest ever achieved in an RTBT. Previously a comparable cut-off frequency was obtained in a RHET with a single collector current peak [42]. Curve (*b*) refers to a bias point between the two peaks. For curve (*c*) instead the base current (40 μA) is such that no NDR appears in the corresponding common-emitter characteristic.

IV. Circuit Applications

A. Frequency Multiplier

The transfer characteristics of Fig. 8 were used to design the frequency multiplier circuit shown in Fig. 12(a). As the input voltage is increased, the collector current increases resulting in a decrease in the collector voltage until the device reaches the negative transconductance regions where sudden drops in the collector current and hence increases in the output voltage are observed. Thus, under suitable bias (V_{BB}), such that the base-emitter junction is biased between the two peaks of the common-emitter transfer characteristic, triangular input waves will be multiplied by a factor of three and sinewaves by a factor of five [23]. Unlike two-terminal multipliers, the output signal in this case is ground referenced and is also isolated from the input. These advantages are obtained in this circuit because the multiple peaks are present in the transfer characteristic of a transistor rather than the *I-V* curve of a two-terminal device as in [35]. It should be noted that, in applications where two-terminal devices cannot be used, conventional frequency-independent multipliers require the use of a phase-lock loop and a digital frequency divider.

The gain of the circuit is determined by the transconductance of the transistor and the collector resistance R_C. However, too large a value for R_C will lead to saturation of the device at large input voltages. The saturation can of course be avoided by the choice of a larger supply voltage V_{CC}, but the maximum usable V_{CC} is presently limited by the collector-base breakdown of the device. In our circuits we had V_{CC} = 3.0 V, V_{BB} = 1.8 V, R_C = 5 Ω, and R_B = 50 Ω. Fig. 12(b) and (c) shows the experimental results of multiplying the frequency of triangular and sinewave inputs, respectively. The polarity of the output signals (bottom traces) are inverted in the display for clarity of presentation.

For frequency multiplication at high frequencies, the devices described in Section III-C were biased in the common-emitter configuration with V_{CE} = 3.2 V and the characteristic impedance of the 50-Ω line as the load. The base-emitter junction was dc biased at 2.0 V via a bias tee. A 350-MHz sinewave was applied to the base. The amplitude was adjusted to achieve a base-emitter voltage swing large enough to bring the device into the negative transconductance regions of the transfer characteristic. The output power versus frequency was displayed on a spectrum analyzer (Fig. 13). Note that the amplitude of the fifth harmonic is much larger than that of the fourth and the sixth. The efficiency of the multiplier (power ratio of the fifth harmonic to the fundamental) is ≈ 15 percent, which is close to the maximum achievable (20 percent) in a resistive multiplier (= $1/n$ where n is the harmonic under consideration).

B. Parity Generator

Fig. 14(a) shows a 4-bit parity generator circuit employing the previously discussed multiple-state RTBT [43]. The voltages of the four input bits of the digital word are added up at the base node of the transistor by the resistive network, to generate a step-like waveform. The quiescent bias of the transistor, adjusted by the resistance R_{B1} and the values of the resistances R_0 are chosen to select the operating points of the transistor alternately at low and high collector current levels (i.e., valleys and peaks of the transfer characteristics) at the successive steps of the summed up voltage. In our circuit, we had R_0 = 15 kΩ, R_{B1} ~ 6.9 kΩ, R_{B2} = 2.4 kΩ, R_C = 15 Ω, and V_{CC} = 4.5 V. The output voltage at the collector would thus

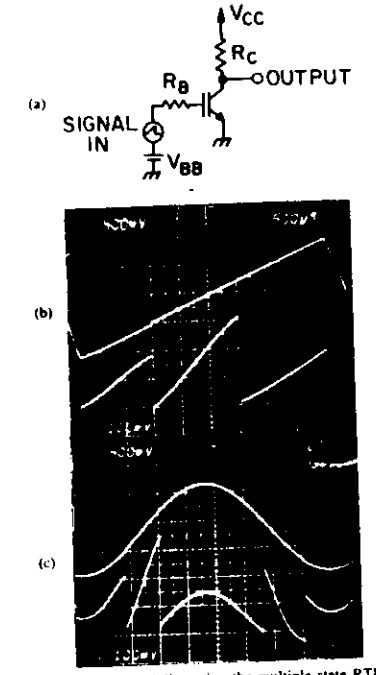

Fig. 12. (a) Frequency multiplier using the multiple-state RTBT and (b) the experimental results of multiplying sawtooth and (c) sine-wave input signals at room temperature.

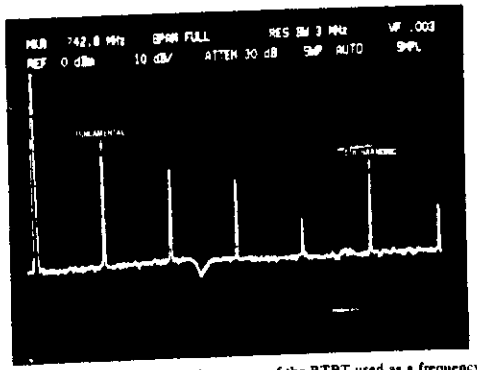

Fig. 13. Power output spectral response of the RTBT used as a frequency multiplier. Vertical scale is −10 dB/div. measured from the top horizontal line (0-dBm reference). The frequency span is 1.8 GHz (180 MHz/div.).

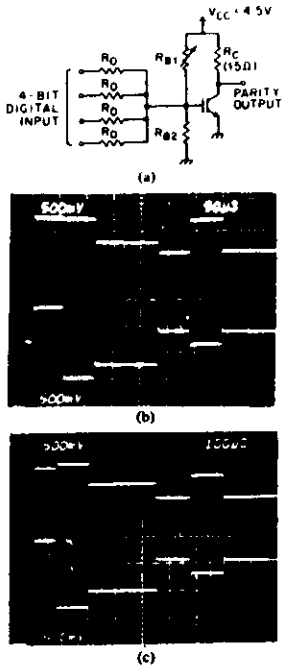

Fig. 14. (a) Four-bit parity generator circuit using an RTBT (R_0 = 15 kΩ, R_{B1} = 6.9 kΩ, R_{B2} = 2.4 kΩ, and R_C = 15 Ω). Note that the same circuit, when used with only two input bits, will act as an exclusive NOR gate. (b) Collector (top trace) and base (bottom trace) waveforms in parity generator circuit at 77 K. (c) Collector (top trace) and base (bottom trace) waveforms at 300 K.

be high or low depending on the number of input bits set high being even or odd, respectively. Thus, we obtain a 4-bit parity generator using only one transistor as compared to the 24 needed in an optimized conventional circuit using three exclusive OR's. Also note that the 4-bit binary data are first converted to a multistate signal that is then processed by the device. This is equivalent to processing all 4 bits in parallel, which results in improved speed compared to conventional sequential processing of binary logic. Such multistate processing elements thus show potential in replacing clusters of circuits in existing binary logic systems. Parity generators using horizontally [35] and vertically integrated [44] RT diodes were demonstrated before. The advantage of the present circuit is that a separate summing amplifier is not required, resulting in further reduction in complexity.

To test the circuit, a pseudorandom sequence of 4-bit binary words was used rather than a monotonically increasing staircase waveform [44], since the latter does not take into account the effect of any hysteresis in the I–V characteristics. Our train of input data produced both positive and negative steps at the base of the transistor. Experimental results at 77 and 300 K are shown in Fig. 14(b) and (c), respectively, where the top traces show the output waveforms and the bottom traces the base waveforms of the transistor. Considering the dotted line in the upper trace as a logic threshold level, we find that the output is low for the second and the fourth voltage levels at the base while it is high for the others. It may also be noted that, at room temperature, the differential transconductance of the device decreases appreciably at higher voltages, making the design of the circuit more critical.

C. Multi-State Memory

A suitable load line drawn on I–V characteristics with n peaks will intersect the later at $n + 1$ points in the positive slope part, as illustrated in Fig. 15 in the case of two peaks [35]. Thus, the circuit shown in the inset of Fig. 15 will have $n + 1$ stable operating points and hence can be used as a memory element in an $n + 1$ state logic system. Even in a binary computer, the storage system could be built around an $n + 1$ logic to increase the packing density, and the data converted to and from binary at the input–output interface. We have demonstrated the above scheme using horizontally integrated RT structures exhibiting two peaks in the I–V as described in [35]. With a supply voltage V_{SS} = 16 V, a load resistance R_L = 215 Ω, and the device biased to V_{BA} = 0.7 V, the three stable states were measured to be at 3.0, 3.6, and 4.3 V. The corresponding load line drawn on the measured characteristic of the device at V_{BA} = 0.7 V intersects at 2.8, 3.4, and 4.1 V, respectively, which are in close agreement with the measured values of the three stable operating points. Similar memory cells utilizing triple-well RT diodes have been demonstrated by Tanoue *et al.* [45].

The three-state memory cell discussed above is also suitable for integration in memory IC's with a READ/WRITE and DECODING network laid out as shown in Fig. 16. The memory cells are placed in a matrix array, and a particular element in the array is addressed by activating the corresponding row and column select lines. A row select connects each device in that row to the corresponding column lines. The column select finally connects the selected column to the data bus. Consider the element (i, j) of the memory matrix shown in Fig. 16. When the row select line is activated, it turns the driving switch Q1 on. It also turns on the switches for every element in the ith row. The column select logic now connects the jth column only to the data bus. The ternary identity cell acts as the buffer between the memory element and the external circuit for reading data. For reading data from the memory, the identity cell is activated with the READ ENABLE line, and data from element number (i, j) in the matrix goes, via the data bus, to the in/out pin of the IC. When the WRITE ENABLE line is activated, data from the external circuit are connected to the data bus and are subsequently forced on the (i, j)th element in the array and are written there.

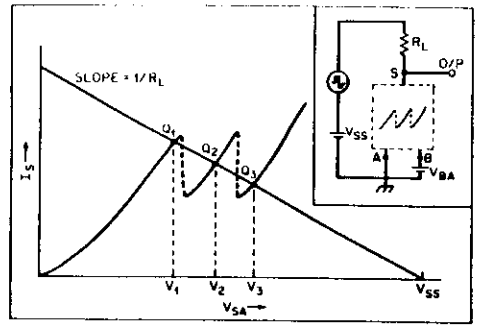

Fig. 15. Schematic of a three-state memory cell. The load line on the I–V shows three stable operating points Q_1, Q_2, and Q_3.

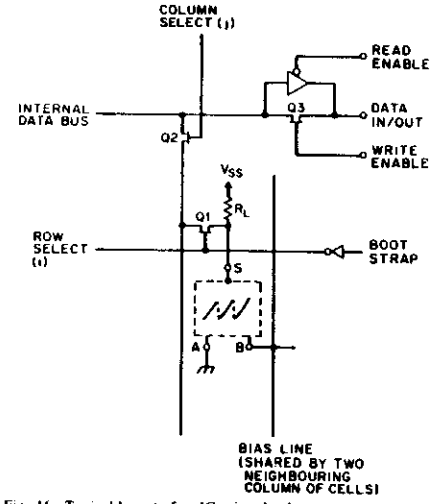

Fig. 16. Typical layout of an IC using the three-state memory cells.

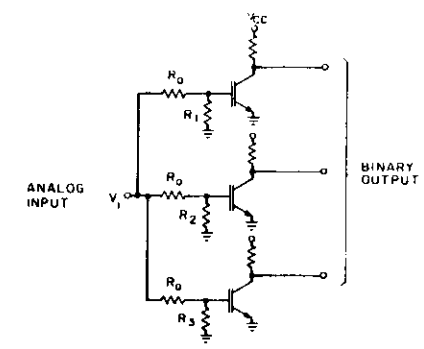

Fig. 17. Analog-to-digital converter circuit using multiple-state RT

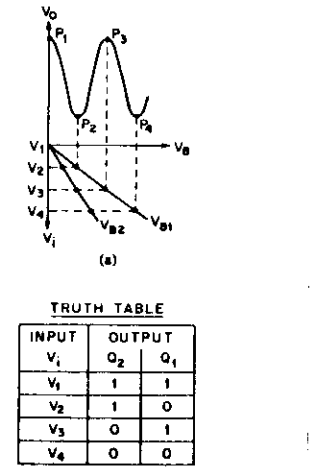

TRUTH TABLE

INPUT V_i	OUTPUT Q_2	Q_1
V_1	1	1
V_2	1	0
V_3	0	1
V_4	0	0

(b)

Fig. 18. The schematic operation of the analog to digital converter of Fig. 17, involving only 2 bits: (a) the voltages at different pc the circuit for various input voltages; (b) the truth table.

D. Analog-to-Digital Converter

Among the other circuit applications of the multi-state RTBT, the analog-to-digital converter, briefly mentioned in [14] and shown in Fig. 17, is potentially the most significant. The analog input is simultaneously applied to an array of RTBT circuits having different voltage scaling networks. To understand the operation of the circuit, consider the simplest system comprised of only two transistors, Q_1 and Q_2. The voltages at different points of this circuit are shown in Fig. 18(a) for various input voltages V_i. Consider that the resistances R_0, R_1, and R_2 are so chosen that the base voltages V_{B1} and V_{B2} of the transistors Q_1 and Q_2 vary with V_i according to the curves V_{B1} and V_{B2}, respectively. With the input voltage at V_1, the output of both of the transistors will be at the operating point P_1 (high state). With the input changing to V_2, the output of Q_1 will become low (P_2), while that of Q still remain high (closer to P_1). Applying this logic input voltages V_3 and V_4, it can be easily shown tha circuit indeed follows the truth table of Fig. 18(b). outputs of the RTBT array thus constitute a binary representing the quantized analog input level. The s can be extended to more bits with a larger number of in the I–V. Note that this is a flash converter req only n transistors for n-bit conversion as compared analog comparators in conventional flash converters. thermore, the array of RTBT's not only works as the parators, but also gives the digital output directly, nating the 2^n-to-n bit decoder needed in conventiona cuits. This further reduces the circuit complexity enhances the speed of operation. However, it is ver

ficult to implement this circuit with the present RTBT's. It should be noted that successful operation of the circuit relies on transfer characteristics where the current remains at a high or low level for a significant span of the base-emitter voltage. In the multi-state RTBT's implemented so far, on the other hand, the current gradually increases with the input voltage and then suddenly drops followed by another gradual rise.

In conclusion, it should be mentioned that, in all of these circuits, the minimum allowable collector voltage is determined by the maximum input signal voltage applied at the base terminal, which is higher than that in a normal bipolar transistor. In fact, in the multiple-state RTBT's demonstrated so far, the QW's are positioned between the base and the emitter contact so that the applied base-to-emitter voltage is used to bias the emitter-base p-n junction *and* the QW's. The base potential is then elevated to a relatively high value under operating conditions in the common-emitter mode. As a result, the quiescent collector bias must be large in order to allow for sufficient output signal swing without forward biasing the collector-base junction. This requires proper care on the part of the circuit designer and careful device design so as to achieve sufficiently high breakdown.

V. Gated Quantum Well and Superlattice Base Transistors

Other than the RHET, several unipolar three-terminal devices have been proposed and implemented utilizing the RT structure to generate voltage tunable NDR and negative transconductance characteristics. In 1985, Luryi and Capasso proposed the quantum wire transistor [46], a device in which the resonant tunneling is of two-dimensional electrons into a one-dimensional quantum well. In 1987, the resonant-tunneling gate field-effect transistor (RT-FET) [47]–[49] was developed at Bell Laboratories. The integration of RT diodes and FET's [50]–[52] and their circuit applications [53] has also been demonstrated.

Bandgap engineering also allows the utilization of RT in other transistor structures. One such structure is the gated QW transistor, demonstrated at Bell Laboratories [54] in 1988. This is the first transistor in which negative transconductance is achieved by directly controlling the potential of the QW.

The structure was proposed by Bonnefoi *et al.* [55] in 1985 under the name of the "Stark effect transistor." The key ideas of that transistor were the use of a QW collector and the inverted sequence of layers in which the controlling electrode (here referred to as the *gate* [54]) was placed "behind" the collector layer. It was predicted that the gate field would modify the position of the collector subbands with respect to the emitter Fermi level and thus modulate the tunneling current. As demonstrated in [54], the structure offers additional advantages, namely NDR and negative transconductance. Moreover, the operation of the device is only partly governed by the Stark effect. In fact another mechanism, *the quantum capacitance* [56], is essential in understanding its operation.

The device grown by MBE in the AlGaAs material system consisted of an undoped quantum-well collector 120 Å thick to which contact was provided. This layer was separated from an n^+-doped emitter by a 40-Å-thick undoped AlAs tunneling barrier. On the other side of the collector, a 1200-Å-thick undoped AlAs barrier was followed by the n^+ gate. The doping of the 5000-Å-thick n^+ layers was nominally 2×10^{18} cm^{-3}. The energy diagram of the device is sketched in Fig. 19.

The emitter-collector I–V characteristics of the device are expected to peak at biases that maximize the RT of the emitter electrons into the 2-D collector subbands. Transistor action in the structure is obtained via the influence of the gate field on the alignment of the 2-D electron gas energy levels relative to the emitter Fermi level. This occurs, as anticipated above, for the combined action of the generalized Stark effect and the quantum capacitance effect. This contribution to the capacitance, not present in a classical metal, arises from the energy that has to be spent in order to raise the Fermi energy in the well, as the carrier concentration is increased by the increasing gate field. This causes the gate field to penetrate beyond the 2-D electron gas in the quantum well and induce charges on the emitter electrode [56].

In Fig. 19 the band diagram of the device is shown in the common-collector configuration with applied biases $V_G > 0$ and $V_E < 0$ such that the bottom of the conduction band in the emitter is in resonance with the second collector subband; this corresponds to a peak in the current. The RT current can be subsequently reduced by increasing either V_E (in modulus) or V_G. The former leads to the observation of NDR, the latter of negative transconductance.

In Fig. 20 experimental data are shown at cryogenic temperature. The expected features are indeed present and were observed, although less pronounced, up to liquid-nitrogen temperature. In particular, the data show for the transconductance a value of the order of $\approx$ 1 mS.

To understand why the peaks in Fig. 20 occur at such high bias V_E, one must consider the potential drop ($I_C R_C$ in Fig. 19) across the series resistance R_C ($\approx$ 1 kΩ) introduced by the exposed part of the collector layer between the emitter mesa and the collector ring contact [54].

As shown in [54], the operation of the device can be modeled quantitatively with great accuracy taking into account the two mechanisms governing this structure.

This device has the advantage of a negligible gate current (it is always several orders of magnitude smaller than the emitter current), which gives a large current transfer ratio but suffers from the drawback of a relative small transconductance.

Negative transconductance can also be obtained using suitably designed minibands in the superlattice base of a transistor. In fact, one of the structures proposed by Capasso and Kiehl [14] consists of an HBT with a superlattice in the base. The emitter is degenerately doped so that electrons can be injected by tunneling into the miniband (Fig. 21(a)). When the base-emitter voltage exceeds the

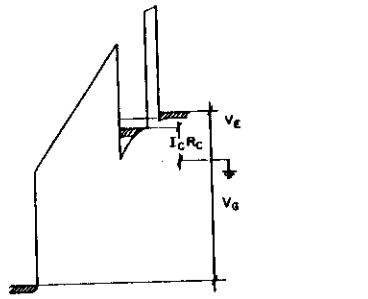

Fig. 19. Band diagram of the gated quantum-well resonant-tunneling transistor with the collector at reference and the biases $V_G > 0$ and $V_E < 0$ corresponding to peak resonant tunneling of emitter electrons into the second subband of the well.

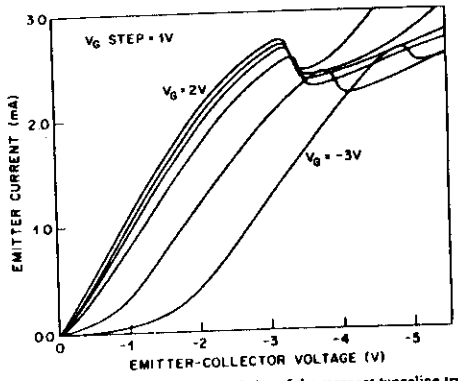

Fig. 20. Common-collector characteristics of the resonant tunneling transistor of Fig. 19 at various V_G (2, 1, 0, −1, −2, −3 V). The measurements were performed at 7 K.

bias required to line up the bottom of the conduction band in the emitter with the top of the miniband (Fig. 21(b)), the collector current is expected to drop. This negative transconductance arises in a straightforward manner from the conservation of lateral momentum and energy during tunneling into the miniband, similar to the situation in RTDB's. This effect has recently been observed by us in an InP/GaInAs superlattice HBT [57].

The structure, grown by chemical-beam epitaxy, is grown on an n^+ (100) InP substrate. An $n = 5 \times 10^{17}$ cm^{-3} 5000-Å $Ga_{0.47}In_{0.53}As$ buffer layer is followed by an undoped n-type $Ga_{0.47}In_{0.53}As$ 1.8-μm-thick collector. The base consists of a p^+ (2×10^{18} cm^{-3}) $Ga_{0.47}In_{0.53}As$ 500-Å-thick region, adjacent to the collector layer, followed by a 20-period $Ga_{0.47}In_{0.53}As$ (70 Å)/InP(20 Å) superlattice. The barrier layers are undoped while all the GaInAs wells are heavily doped (2×10^{18} cm^{-3}) p-type. A 20-Å undoped InP doping set back layer separates the superlattice from the 5000-Å-thick n^+ ($\approx 2 \times 10^{18}$ cm^{-3}) InP emitter. This superlattice design ensures the formation of relatively wide minibands, in order to guarantee Bloch conduction of injected electrons through the base. The calculations show that the ground state electron miniband extends from 36.6 to 75.2 meV, while the heavy hole miniband extends from 11.9 to 12 meV. Energies are measured from the classical bottom of the conduction and valence band wells, respectively. Conduction band nonparabolicities were included in these envelope function-type calculations; $\Delta E_c = 0.23$ eV and $\Delta E_c = 0.37$ eV were used for the band discontinuities.

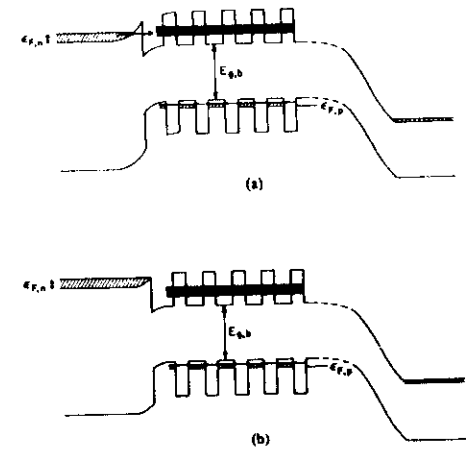

Fig. 21. Band diagram of superlattice base HBT (a) under injection conditions into the miniband and (b) at the onset of negative transconductance.

Fig. 22 shows the common-base transfer characteristics at 7 and 77 K. Consider first the collector current at 7 K. At these low temperatures thermionic emission from the emitter is completely negligible, and injection from the emitter is dominated by tunneling. From the band diagram (Fig. 21) it is clear then that only a small electron current (zero at 0 K in the absence of band tailing) can flow from the emitter into the base until the quasi-Fermi energy in the emitter is lined up with the bottom of the miniband. This requires a bias V_{EB} equal to $(\epsilon_{F,p} + E_{1,hh} + E_{g,b} + E_{1,e})/e = 0.876$ V, where $\epsilon_{F,p}$ is the Fermi energy in the base (= 15 meV), $E_{1,hh}$ the bottom of the heavy hole miniband (= 12 meV), $E_{g,b}$ the GaInAs bulk bandgap (= 0.812 eV), and E_{1e} the bottom of the first electron miniband (= 36.6 meV). The data of Fig. 22 indeed show that the collector current rapidly increases for $V_{BE} > 0.86$ V, in good agreement with the calculated onset voltage.

The suppression of injection into the miniband requires increasing the emitter-base voltage by $> \Delta E_1 + \epsilon_{F,n} = 118.6$ meV where $\Delta E_1 = 38.6$ meV is the width of the first electron miniband and $\epsilon_{F,n} = 80$ meV is the quasi-Fermi energy in the emitter. Thus, the onset of negative transconductance (voltage position of the peak) is expected to be at 0.994 V, in excellent agreement with the

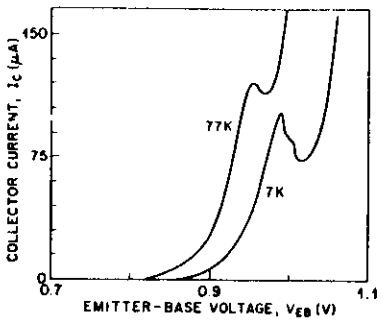

Fig. 22. Transfer characteristic of the superlattice base HBT in the common base configuration at two different temperatures. The collector-base bias is −2 V.

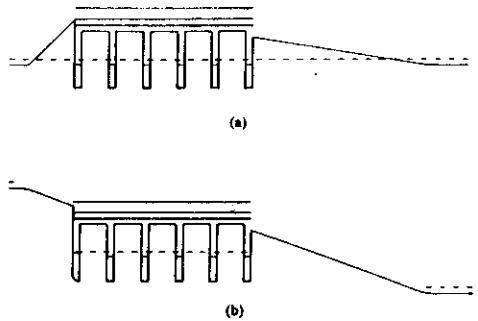

Fig. 23. Conduction-band energy diagram of the superlattice-base transistor: (a) at equilibrium and (b) in the common-base configuration near the peak of the current–voltage characteristic. Further increase in the negative emitter-base bias will suppress injection in the base due to quantum reflections by the minigap.

experimental value (≈ 0.99 V). Following the drop in the collector current, the latter rises rapidly for $V \geq 1.02$ V. This is expected, since at a bias $\approx E_g + \Delta E_c \approx 1.03$ V the conduction band edge in the emitter becomes flat, leading to a steep increase in the injection efficiency. Note that at 77 K the peak shifts to a lower voltage. The shift (≈ 25 mV) is close, as expected, to the GaInAs bandgap lowering (≈ 30 meV) as the temperature is varied from 7 to 77 K.

The common-base characteristics I_C, I_E versus V_{EB} showed a maximum base transport factor $\alpha = I_C/I_E = 0.75$ at $V_{BE} \approx 0.98$ V. This value is consistent with the maximum gain $\beta = I_C/I_B \simeq 3.3$ measured in the common-emitter configuration. These values of α and β, although far from optimal, indicate that transport in the base is via miniband conduction rather than hopping. Previously Palmier *et al.* had reported an HBT with an AlGaAs/GaAs superlattice base [58]. Although miniband conduction in the base was demonstrated, no negative transconductance was shown since the structure did not use a tunneling emitter for injection.

Negative transconductance can also be achieved by controlling injection into minibands above the top of the barriers. Recently, Lent proposed a tunneling-emitter transistor in which hot electrons transfer through the base by miniband conduction in a continuum state [59]. Here we present the operation of a new superlattice base unipolar transistor in which electrons are injected into a miniband in the classical continuum [60].

The structure, whose equilibrium conduction band energy diagram is sketched in Fig. 23(a), was grown by MBE. It consists of an 8000-Å n^+ collector followed by an undoped $Al_xGa_{1-x}As$ layer 5000 Å thick with x varying from 0 to 0.25. On top of these the SL base was grown, consisting of 5.5 periods of 40-Å n^+ GaAs/200-Å undoped $Al_{0.31}Ga_{0.69}As$. An undoped $Al_xGa_{1-x}As$ injector layer 500 Å thick followed with x varying from 0 to 0.33, corresponding to a band discontinuity $\Delta E_c = 273$ meV, roughly, at the bottom of the chosen miniband. Finally, an n^+ emitter layer 3000 Å thick concluded the growth. In all the doped layers, $n = 2 \times 10^{18}$ cm^{-3}.

The operation of the device is easily understood with the help of Fig. 23 where the common-base operation mode is illustrated. At a fixed positive collector-base bias, the negative emitter-base bias (V_{EB}) is increased and the collector current is measured. By appropriately tailoring the compositionally graded emitter barrier, electrons are injected into the third miniband. The energy dispersion of the latter was calculated in the envelope function approximation taking into account band nonparabolicities and is large enough (≈ 23 meV) to guarantee miniband conduction. Increasing V_{EB} will further flatten the triangular injector and increase the injection current. However, part of the bias will appear in a depletion region in the base, thus shifting the top of the band discontinuity with respect to the miniband. When this shift is larger than the miniband width, the injected electrons will not be able to satisfy the energy and lateral momentum conservation conditions at the interface and will experience strong quantum mechanical reflections. Consequently, the injection efficiency will drop together with the collector current, and the I–V characteristic will exhibit negative transconductance. This effect is shown in the experimental curves shown in Fig. 24. In fact, a 23-meV shift (≈ miniband width) of the top of the injector band discontinuity is required to suppress electron injection. This corresponds to an almost total depletion of the first well of the base and gives by a simple electrostatic computation an emitter-base bias of ≈ 0.6 V in agreement with the peak position for $V_{CB} < 0$ (Fig. 24).

In the present structure the base transport factor is $\ll 1$ leading to a small I_C. Optimization of the design and elimination of stray leakage paths must be achieved in order to enhance α.

The structures discussed in this section are of interest primarily from a physics point of view as tools to investigate transport in two-dimensional systems and superlattices. Their operation so far has only been demonstrated at cryogenic temperatures. Performance-wise, these devices have several shortcomings in comparison with the much more advanced RTBT's described in the preceding sections.

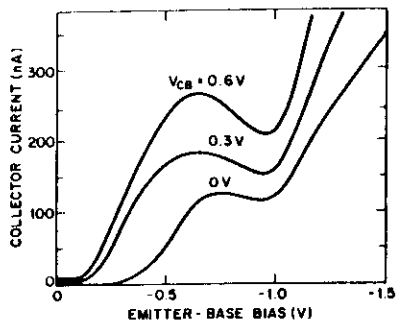

Fig. 24. Collector current as a function of emitter-base bias at fixed collector-base (V_{CB}) bias at 30 K.

Acknowledgment

The authors are grateful to D. Sivco for the growth of some of the structures, to W. T. Tsang for the growth of the superlattice HBT wafer, and to A. L. Hutchinson for processing the superlattice transistors. Collaborations and useful discussions with J. Allam, R. Kiehl, D. V. Lang, S. Luryi, and M. Shoji are also gratefully acknowledged.

References

[1] J. A. Morton, "From physics to function," *IEEE Spectrum*, p. 62, Sept. 1965.
[2] L. Esaki, "New phenomenon in narrow germanium *p-n* junctions," *Phys. Rev.*, vol. 109, p. 603, 1958.
[3] W. S. Boyle, and G. E. Smith, "Charged-coupled semiconductor devices," *Bell Syst. Tech. J.*, vol. 49, p. 587, 1970.
[4] F. Capasso, "Graded-gap and superlattice devices by bandgap engineering," in *Semiconductors and Semimetals*, vol. 24, R. K. Willardson and A. C. Beers, Eds. New York: Academic, 1987, p. 319.
[5] D. A. B. Miller *et al.*, "Novel hybrid optically bistable switch: The quantum well self-electro-optic effect device," *Appl. Phys. Lett.*, vol. 45, p. 13, 1984.
[6] L. L. Chang, L. Esaki, and R. Tsu, "Resonant tunneling in semiconductor double barriers," *Appl. Phys. Lett.*, vol. 24, p. 593, 1974.
[7] T. C. L. G. Sollner, W. D. Goodhue, P. E. Tannenwald, C. D. Parker, and D. D. Peck, "Resonant tunneling through quantum wells at frequencies up to 2.5 THz," *Appl. Phys. Lett.*, vol. 43, p. 588, 1983.
[8] E. R. Brown, T. C. L. G. Sollner, C. D. Parker, W. D. Goodhue, and C. L. Chen, "Oscillations up to 420 GHz in GaAs/AlAs resonant tunneling diodes," *submitted to Appl. Phys. Lett.*
[9] T. P. E. Broekaert, W. Lee, and C. G. Fonstad, "Pseudomorphic $In_{0.53}Ga_{0.47}As/AlAs/InAs$ resonant tunneling diodes with peak-to-valley current ratios of 30 at room temperature," *Appl. Phys. Lett.*, vol. 53, p. 1545, 1988.
[10] E. R. Brown, T. C. L. G. Sollner, W. D. Goodhue, and C. L. Chen, "High speed resonant tunneling diodes," *Proc. SPIE*, vol. 943, p. 2, 1989.
[11] F. Capasso, S. Sen, F. Beltram, and A. Y. Cho, "Resonant tunneling devices and their applications," in *Submicron Integrated Circuits*, R. K. Watts, Ed. New York: Wiley, 1989, chap. 5.
[12] R. H. Davis and H. H. Hosack, "Double barrier in thin film triodes", *J. Appl. Phys.*, vol. 34, p. 864, 1963.
[13] L. V. Iogansen, "The possibility of resonance transmission of electrons in crystals through a system of barriers," *Zh. Eksp. Teor. Fiz.*, vol. 45, p. 207, 1963. (English trans., *Sov. Phys. JETP*, vol. 18, p. 46, 1964).
[14] F. Capasso and R. A. Kiehl, "Resonant tunneling transistor with quantum well base and high-energy injection. A new negative differential resistance device," *J. Appl. Phys.*, vol. 58, p. 1366, 1985.
[15] B. Riccò and P. M. Solomon, "Tunable resonant tunneling semiconductor emitter structure," *IBM Tech. Dig. Bull.*, vol. 27, p. 30, 1984.
[16] R. T. Bate, G. A. Frazier, W. R. Frensley, J. K. Lee, and M. Reed, *Proc. SPIE*, vol. 792, p. 26, 1987.
[17] N. Yokoyama, K. Imamura, S. Muto, S. Hiyamizu, and H. Nis "A new functional resonant tunneling hot electron transis (RHET)," *Japan J. Appl. Phys.*, vol. 24, p. L-853, 1985.
[18] N. Yokoyama, *et al.*, "Resonant-tunneling transistors using InGa based materials," *Proc. SPIE*, vol. 943, p. 14, 1988.
[19] F. Capasso, S. Sen, A. C. Gossard, A. L. Hutchinson, and J. English, "Quantum well resonant tunneling bipolar transistor op ating at room temperature," *IEEE Electron Device Lett.*, vol. ED 7, p. 573, 1986.
[20] T. Futatsugi *et al.*, "A resonant tunneling bipolar transistor (RB A proposal and demonstration for new functional device with hi current gains," in *IEDM, Tech. Dig.*, 1986, p. 286.
[21] T. Inata *et al.*, "Excellent negative differential resistance of AlAs/InGaAs resonant tunneling barrier structure grown by MBE *Japan. J. Appl. Phys.*, vol. 25, p. 983, 1986.
[22] F. Capasso, S. Sen, A. Y. Cho, and D. L. Sivco, "Multiple negat transconductance and differential conductance in a bipolar transis by sequential quenching of resonant tunneling," *Appl. Phys. Le* vol. 53, p. 1056, 1988.
[23] S. Sen, F. Capasso, A. Y. Cho, and D. L. Sivco, "Multiple st resonant tunneling bipolar transistor operating at room temperat and its application as a frequency multiplier," *IEEE Electron Dev Lett.*, vol. 9, p. 533, 1988.
[24] C. Rine, Ed., *Computer Science and Multiple-valued Logic*. A sterdam, North Holland, 1977, p. 101.
[25] S. Sen *et al.*, "Observation of resonant tunneling through a com sitionally graded parabolic quantum well," *Appl. Phys. Lett.*, v 51, p. 1428, 1987.
[26] F. Capasso, K. Mohammed, and A. Y. Cho, "Resonant tunnel through double barriers, perpendicular quantum transport phenom in superlattices, and their device applications," *IEEE J. Quant Electron.*, vol. QE-22, p. 1853, 1986.
[27] A. F. J. Levi, "Scaling ballistic heterojunction bipolar transistor *Electron. Lett.*, vol. 24, p. 1273, 1988.
[28] T. Weil and B. Vinter, "Equivalence between resonant tunneling sequential tunneling in double-barrier diodes," *Appl. Phys. Lett.*, v 50, p. 1281, 1987.
[29] R. J. Malik, R. Nottenburg, E. F. Schubert, J. F. Walker, and R. Ryan, "Carbon doping in molecular beam epitaxy of GaAs fro heated graphite filament," *Appl. Phys. Lett.*, vol. 53, p. 2661, 19
[30] A. F. J. Levi, S. L. McCall, and P. M. Platzman, "Nonrandom d ing and elastic scattering of carriers in semiconductors," *Appl. Ph Lett.*, vol. 54, p. 940, 1989.
[31] A. F. J. Levi and Y. Yafet, "Non equilibrium electron transport bipolar devices," vol. 51, p. 42, 1987.
[32] E. Wolak *et al.*, "Elastic scattering centers in resonant tunnel diodes," *Appl. Phys. Lett.*, vol. 53, p. 201, 1988.
[33] F. Capasso, S. Sen, A. Y. Cho, and A. L. Hutchinson, "Reson tunneling spectroscopy of hot minority electrons injected in galli arsenide quantum wells," *Appl. Phys. Lett.*, vol. 50, p. 930, 198
[34] M. A. Reed, W. F. Frensley, R. J. Matyi, J. N. Randall, and A. Seabaugh, "Realization of a three terminal resonant tunneling devi The bipolar quantum resonant tunneling transistor," *Appl. Phys. Le* vol. 54, p. 1034, 1989.
[35] S. Sen, F. Capasso, A. Y. Cho, and D. Sivco, "Resonant tunnel device with multiple negative differential resistance: Digital and s nal processing applications with reduced circuit complexity," *IE Trans. Electron. Devices*, vol. ED-34, p. 2187, 1987.
[36] J. Söderström and T. G. Andersson, "A multiple-state memory based on the resonant tunneling diode," *IEEE Electron Device Le* vol. 9, p. 200, 1988.
[37] R. C. Potter, A. A. Lakhani, D. Beyea, E. Hempling, and A. Fat mulla, "Three-dimensional integration of resonant tunneling str tures for signal processing and three-state logic," *Appl. Phys. Le* vol. 52, p. 2163, 1988.
[38] S. Sen, F. Capasso, D. Sivco, and A. Y. Cho, "New resonant t neling devices with multiple negative resistance regions and high ro temperature peak to valley ratio," *IEEE Electron Device Lett.*, v 9, p. 402, 1988.
[39] *General Electric Tunnel Diode Manual*, 1st ed., 1961, p. 66.

[40] M. Tsuchiya, H. Sakaki, and J. Yoshino, "Room temperature observation of differential negative resistance in an AlAs/GaAs/AlAs resonant tunneling diode," *Japan. J. Appl. Phys.*, vol. 24, p. L466, 1985.
[41] L. M. Lunardi *et al.*, "Microwave multiple-state resonant tunneling bipolar transistor," *IEEE Electron Device Lett.*, vol. 10, p. 219, 1989.
[42] T. Mori, "Microwave analysis of resonant tunneling hot electron transistor at room temperature," in *Extended Abstracts 20th Conf. Solid State Devices and Materials* (Tokyo), 1988, p. 507.
[43] S. Sen, F. Capasso, A. Y. Cho, and D. L. Sivco, "Parity generator circuit using a multi-state resonant tunneling bipolar transistor," *Electron. Lett.*, vol. 24, p. 1506, 1988.
[44] A. A. Lakhani, R. C. Potter, and H. S. Hier, "Eleven-bit parity generator with a single, vertically integrated resonant tunneling device," *Electron. Lett.*, vol. 24, p. 681, 1988.
[45] T. Tanoue, H. Mizuta, and S. Takahashi, "A triple well resonant tunneling diode for multiple valued logic applications," *IEEE Electron Dev. Lett.*, vol. 9, p. 365, 1988.
[46] S. Luryi and F. Capasso, "Resonant tunneling of two dimensional electrons through a quantum wire: A negative transconductance device," *Appl. Phys. Lett.*, vol. 47, p. 1347, 1985; also, Erratum, *Appl. Phys. Lett.*, vol. 48, p. 1693, 1986.
[47] F. Capasso, S. Sen, F. Beltram, and A. Y. Cho, "Resonant tunneling gate field-effect transistor," *Electron. Lett.*, vol. 23, p. 225, 1987.
[48] S. Sen, F. Capasso, F. Beltram, and A. Y. Cho, "The resonant tunneling field-effect transistor: A new negative transconductance device," *IEEE Trans. Electron Devices*, vol. ED-34, p. 1768, 1987.
[49] F. Capasso, S. Sen, and A. Y. Cho, "Negative transconductance resonant tunneling field effect transistor," *Appl. Phys. Lett.*, vol. 51, p. 526, 1987.
[50] A. R. Bonnefoi, T. C. McGill, and R. D. Burnham, "Resonant tunneling transistors with controllable negative differential resistance," *IEEE Electron Device Lett.*, vol. EDL-6, p. 636, 1985.
[51] T. K. Woodward, T. C. McGill, and R. D. Burnham, "Experimental realization of a resonant tunneling transistor," *Appl. Phys. Lett.*, vol. 50, p. 451, 1987.
[52] T. K. Woodward, T. C. McGill, H. F. Chung, and R. D. Burnham, "Integration of a resonant-tunneling structure with a metal-semiconductor field-effect transistor," *Appl. Phys. Lett.*, vol. 51, p. 1542, 1987.
[53] ——, "Applications of resonant-tunneling field-effect transistors," *IEEE Electron Device Lett.*, vol. 9, p. 122, 1988.
[54] F. Beltram, F. Capasso, S. Luryi, S. N. G. Chu, and A. Y. Cho, "Negative transconductance via gating of the quantum well subbands in a resonant tunneling transistor," *Appl. Phys. Lett.*, vol. 53, p. 219, 1988.
[55] A. R. Bonnefoi, D. H. Chow, and T. C. McGill, "Inverted base-collector tunnel transistors," *Appl. Phys. Lett.*, vol. 47, p. 888, 1985.
[56] S. Luryi, "Quantum capacitance devices," *Appl. Phys. Lett.*, vol. 52, p. 501, 1988.
[57] F. Capasso, A. S. Vengurlekar, A. L. Hutchinson, and W. T. Tsang, "A negative transconductance superlattice base bipolar transistor," *Electron. Lett.*, vol. 25, p. 117, 1989.
[58] J. F. Palmier *et al.*, "Observation of Bloch conduction perpendicular to the interfaces in a superlattice bipolar transistor," *Appl. Phys. Lett.*, vol. 49, p. 1260, 1986.
[59] C. S. Lent, "The resonant hot electron transfer amplifier: A continuum resonance device," *Superlattices and Microstructures*, vol. 3, p. 387, 1987.
[60] F. Beltram, F. Capasso, A. L. Hutchinson, and R. J. Malik, "Continuum miniband superlattice-base transistor with graded-gap electron injector," *Electron. Lett.*, vol. 25, p. 1219, 1989.

*

Federico Capasso (M'79-SM'85-F'87) received the Doctor of Physics degree (*summa cum laude*) from the University of Rome, Rome, Italy, in 1973. His dissertation concerned stimulated Raman spectroscopy.

He was a Research Scientist at the Fondazione Bordoni from 1974 to 1976, working on the theory of nonlinear phenomena in optical fibers and on dye lasers. He joined AT&T Bell Laboratories, Murray Hill, NJ, in 1976 where he has engaged in research on impact ionization, 1.3- to 1.6-μm detectors, liquid-phase epitaxy of III-V materials, surface passivation and defect studies, high-field transport in semiconductors, novel avalanche photodiode structures, bipolar transistors, variable-gap heterostructures, resonant tunneling, and superlattices. He pioneered the technique of band-gap engineering and has used it extensively in the design of a new class of superlattice and heterojunction devices. He is currently Head of the Quantum Phenomena and Device Research Department at Bell Labs. He has given 70 invited talks at conferences in the U.S. and abroad and has co-authored over 130 papers.

Dr. Capasso received the AT&T Bell Labs Distinguished Member of Technical Staff Award and the Award of Excellence of the Society for Technical Communication in 1984. He is a fellow of the American Physical Society and the Optical Society of America. He has been serving on the program committees of numerous international conferences. He was Program Co-chairman of the 1987 Topical Meeting on Picosecond Optoelectronics and Electronics, Chairman of the Solid State Detector Technical Group of the Optical Society of America, and Co-chairman of the 1988 and 1990 Symposium on Advances in Semiconductors and Superconductors. He is an Associate Editor of *Photonics Technology Letters*.

*

Susanta Sen (M'87) was born in Calcutta, India on December 30, 1951. He received the B.Sc degree in physics (Honors) and the B.Tech., M.Tech., and Ph.D. degrees in radio physics and electronics from the University of Calcutta, Calcutta, in 1970, 1973, 1975, and 1983, respectively.

From 1976 to 1978, he worked as a C.S.I.R. Research Fellow. He joined the Institute of Radio Physics and Electronics, University of Calcutta as a Lecturer in 1978 and became a Reader in 1985. His research interests include electronic instrumentation, microwave measurements, III-V compound semiconductor crystal growth (LPE), and quantum electronic devices. Since February 1986, he has been with AT&T Bell Laboratories, Murray Hill, NJ. At Bell Labs, he is working on resonant-tunneling structures and their device applications using bandgap engineering. In 1989, he returned to the University of Calcutta where he has been appointed Full Professor.

Dr. Sen is a founder member of the Semiconductor Society (India).

*

Fabio Beltram (M'87) was born in Italy on June 9, 1959. He received the Doctor of Electronic Engineering degree (*summa cum laude*) from the University of Trieste, Trieste, Italy, and the Doctor of Physics degree (*summa cum laude*) from the University of Bologna, Bologna, Italy.

Beginning in 1984, he worked at C.N.R.-LAMEL in Bologna, first completing his dissertation, then with a fellowship from S.G.S.-Thomson Industries. His studies focused on transport properties and breakdown of ultrathin silicon dioxide and nitrided silicon dioxide insulating layers in metal-insulator semiconductor devices. He has been at AT&T Bell Laboratories, Murray Hill, NJ, since September 1986 as a Consultant-Member of Technical Staff in the Quantum Phenomena and Device Research Department working on optical and electronic transport properties of superlattices and multiquantum-well structures and on heterostructure devices.

Dr. Beltram is member of the American Physical Society and the New York Academy of Sciences.

*

Leda M. Lunardi (S'84-M'85) received the B.Sc. and M.Sc. degrees in physics from the University of São Paulo, São Paulo, Brazil, in 1976 and 1979, respectively, and the Ph.D. degree in electrical engineering from Cornell University, Ithaca, NY, in 1985. Her doctoral dissertation work was on the fabrication of microwave Al GaAs/GaAs heterojunction bipolar transistors.

Since joining AT&T Bell Laboratories in 1985, she has been engaged in research on heterojunction bipolar devices including the design, layout, processing, and characterization for circuits applications. She also has been working on the development and implementation of HBT's in small-scale integration. Her current interests include processing of novel device structures such as the resonant-tunneling bipolar transistor.

Dr. Lunardi is a member of the American Physical Society and the IEEE Electron Devices Society.

Arvind S. Vengurlekar (M'89), photograph and biography not available at the time of publication.

*

Peter R. Smith received the B.S.E.E. degree in 1972 from Northeastern University, and the M.S.(EE) degree in 1975 and the Electrical Engineer (professional) degree in 1977, both from Columbia University.

He is a member of technical staff in the Heterostructure Integrated Circuits and Materials Department at AT&T Bell Laboratories, Murray Hill, New Jersey. Prior to this position he spent eleven years in the High Speed Materials and Phenomena Research Department developing opto-electronic measurement techniques with picosecond time resolution. His present research interests include the application of these high speed measurement techniques to the characterization and modeling of fast devices and circuits.

*

Nitin J. Shah (M'88) was born in Thomson's Falls, Kenya, in 1957. He received the B.A. degree in materials science in 1979, the M.A. degree in 1982, and the Ph.D. degree in microcircuit engineering in 1983, all from the University of Cambridge, England. His doctoral work was on the electron-beam annealing of ion-implanted gallium arsenide.

He joined AT&T Bell Laboratories in 1983, and he is currently the Supervisor of the Heterostructure Integrated Circuits Group. He is responsible for the development of ultra high-speed electronic devices and circuits, in both heterostructure field-effect and heterostructure bipolar transistor technologies. He is also involved in ultra-high-speed characterization using electro-optic techniques and in optical switching devices.

Roger J. Malik (S'80-M'81), photograph and biography not available at the time of publication.

*

Alfred Y. Cho (S'57-M'60-SM'79-F'81) received the B.S., M.S., and Ph.D. degrees in electrical engineering from the University of Illinois in 1960, 1961, and 1968, respectively.

He is Director of the Materials Processing Research Laboratory at AT&T Bell Laboratories, Murray Hill, NJ. He joined Bell Laboratories in 1968 where he developed a crystal growth technology called molecular-beam epitaxy (MBE). His many significant research accomplishments include the construction of surface phase diagram for MBE crystal growth, the first fabrication of an MBE artificial superlattice, the first MBE IMPATT diode, mixer diode, and field-effect transistor operating at microwave frequencies, and the first MBE double-heterostructure laser operating CW at room temperature. His recent work is in the area of quantum-well devices. He has published over 250 papers in surface physics, crystal growth, and device physics and performance. He holds 43 patents on crystal growth and semiconductor devices related to MBE.

Dr. Cho is a recipient of the Electronics Division Award of the Electrochemical Society (1977), the American Physical Society International Prize for New Materials (1982), the IEEE Morris N. Liebmann Award (1982), the University of Illinois Electrical and Computer Engineering Distinguished Alumnus Award (1985), the Chinese Institute of Engineers USA Distinguished Achievement Award (1985), the GaAs Symposium Award-Ford (1986), the Heinrich Welker Medal-Siemens (1986), the Solid State Science and Technology Medal of the Electrochemical Society (1987), the College of Engineering Alumni Honor Award of the University of Illinois (1988), the World Materials Congress Award of ASM International (1988), the Gaede-Langmuir Award of the American Vacuum Society (1988), and the Industrial Research Institute Achievement Award of the Industrial Research Institute, Inc. (1988). He is a Fellow of the American Physical Society, and the American Academy of Arts and Sciences. He is a member of the American Vacuum Society, the Electrochemical Society, the Materials Research Society, the National Academy of Engineering, and the National Academy of Sciences.

to appear in
Phys Rev. Lett.
June 4 1990

Scattering-controlled transmission resonances and negative differential conductance by field-induced localization in superlattices

Fabio Beltram, Federico Capasso, Deborah L. Sivco,
Albert L. Hutchinson, Sung-Nee G. Chu, and Alfred Y. Cho

AT&T Bell Laboratories, Murray Hill, NJ 07974

ABSTRACT

The first observation of scattering-controlled transmission resonances in superlattices is reported. These originate from states supported by subsets of the superlattice of thickness equal to the electron coherence length. At lower electric fields a broad region of negative differential conductance (NDC) due to progressive field-induced wavefunction localization is also observed. This phenomenon is shown to be physically equivalent to the Bragg-diffraction induced NDC predicted by Esaki and Tsu in 1970.

PACS numbers: 73.20.Dx, 73.40Gk, 73.50.Fq.

Scattering-controlled transmission resonances and negative differential conductance by field-induced localization in superlattices

Fabio Beltram, Federico Capasso, Deborah L. Sivco,
Albert L. Hutchinson, Sung-Nee G. Chu, and Alfred Y. Cho

Since the original proposal of superlattices (SLs) by Esaki and Tsu,[1] transport in these structures has been the object of intense investigations. When an electric field F is applied to a SL of period a, some different transport regimes are commonly identified.[2] At low fields, the current increases linearly with field (mobility regime). The current is expected to decrease with increasing field when the electron distribution probes the non-parabolic part of the miniband, i.e., according to Esaki and Tsu[1], for

$$F > \frac{\hbar}{ea\tau}, \tag{1}$$

where τ is the scattering time and e the electron charge. This behavior is caused by the fact that an increasing fraction of the carriers approaches the minizone boundary therefore undergoing Bragg diffraction. Equation 1 was shown to hold independently of the details of the miniband energy dispersion relation.[3]

Another regime was studied by Tsu and Döhler[4] who considered the case of strong localization in a tight-binding SL (i.e. a SL with weak coupling between wells). They showed that due to the decreasing overlap between the wavefunctions of adjacent wells, the transition rate due to hopping (and therefore the current) decreases with increasing field for

$$F > \frac{\Delta E}{ea}, \qquad (2)$$

where ΔE is the miniband width.

In this letter we present direct evidence of negative differential conductance (NDC) by electric-field-induced localization in SLs and show that this mechanism and the Bragg-diffraction induced NDC predicted by Esaki and Tsu are physically equivalent. Furthermore we report the first observation of new resonances that are determined by scattering.

One must not be led to the incorrect notion that Eq. 2 is a *necessary* requirement for the observation of localization in transport.[5-7] Even for fields much lower than those causing the complete localization mentioned above, a progressive localization of the electronic states is to be expected. As originally discussed by Wannier,[8] and subsequently by Kazarinov and Suris[9] in the context of transport in SLs, in an electric field the electronic wavefunctions extend over a number of periods of the order of $\Delta E/eaF$ and are separated in energy by eaF (the so called Wannier-Stark ladder, Fig. 1a). Thus, as the field is increased the wavefunctions become increasingly localized in space up to the extreme point where they are shrunk to one well. This is the limit of Eq. 2 in which the SL consists of a "ladder" of identical isolated quantum wells (Fig. 1b). A decrease in the current is expected throughout this regime since the spatial overlap between the Stark-ladder states decreases with increasing field and with it the matrix element for transitions. Complete localization leading to Stark-ladder quantization was shown by the optical experiments of Mendez et al.[10]

and Voisin et al.[11] These experiments also clearly demonstrate the progressive nature of electric field induced localization. The question then arises, what is the threshold for localization?

Localization will occur when the energy levels of the Stark ladder can be resolved. In the presence of collisions this happens when their separation is greater than the collision broadening, i.e. $eaF > \hbar/\tau$. Therefore, in this physical picture, the threshold for the observation of NDC is $F > \hbar/ea\tau$. This is the same field calculated by Esaki and Tsu for the onset of NDC in a SL (Eq. 1). In fact these two pictures for NDC are equivalent. One must note that the localization condition $eaF > \hbar/\tau$ implies a mean free path greater than $\Delta E/eF$ so that electrons can reach the minizone boundary and undergo Bragg diffraction leading to NDC[12] (the Esaki-Tsu mechanism[1]). (Concerning the k-space derivation of Eq. 1 by Esaki and Tsu,[1] it should be noted that their approach is valid for fields F such that $eaF \ll \Delta E$, so that a semiclassical treatment is applicable.) Yakolev[13] investigated the conductivity of electrons in semiconductors with narrow ($\sim$ 0.1 eV) bands in strong electric fields. Although this paper was written before the introduction of the SL concept, its results are applicable to describe transport in these structures. Yakolev indeed found that for fields satisfying Eq. 1, the conductivity decreases with increasing field. Moreover, as expected from the above discussion, his results are identical to the asymptotic results found by Tsu and Döhler.[4]

These theoretical predictions are experimentally verifiable by simply measuring the current-voltage characteristics of SLs: starting at a bias defined

by Eq. 1, a wide region where the current decreases with increasing voltage would be the signature of the localization. This observation, however, has not been reported yet.[14] Recently, negative differential velocity (*not* negative differential conductance) has been inferred from microwave measurements in GaAs/AlAs SLs[7] and attributed to the Esaki-Tsu mechanism.

In our opinion, one of the main problems hindering the experimental study of electronic transport in SLs has been the interdependence of the intensity of the current injected and the field present in the SL which is unavoidable in the 2-terminal structures studied so far. At higher fields the large current densities injected make the field in the SL nonuniform and cause the formation of high field domains.[15,16] Therefore we designed a 3-terminal structure that could simulate as closely as possible the "ideal" situation: a monoenergetic beam of electrons of constant flux current impinging on the SL, independent of the value of the field in the SL. The equilibrium band-diagram of our structure is schematically drawn in Fig. 2a. The forward-biased p-n "emitter" heterojunction provides a controllable source of current independent of the reverse bias applied to the "collector" heterojunction which in turn controls the field in the SL. By measuring the "collector" current at constant "emitter" current we can test the "intrinsic" SL transport properties as a function of a uniform SL field avoiding the complications mentioned above. The undoped collector region between the SL and the contacted n^+ layer serves the purpose of scaling the applied bias.

The structures were grown by molecular beam epitaxy lattice matched on an undoped InP substrate. The growth started with a 4955-Å $Ga_{0.47}In_{0.53}As$ buffer

layer doped $n^+ = 1\times10^{18}$ cm^{-3} followed by a 5945 Å thick $Ga_{0.47}In_{0.53}As$ undoped collector region. The SL was then grown followed by a 5000-Å $Al_{0.163}Ga_{0.312}In_{0.525}As$ layer doped $p^+ = 5\times10^{18}$ cm^{-3}. Finally 850-Å $Al_{0.48}In_{0.52}As$ $n^+ = 5\times10^{17}$ cm^{-3} was grown separated by a 300-Å quaternary graded region from the $Ga_{0.47}In_{0.53}As$ $n^+ = 1\times10^{19}$ cm^{-3} 2000-Å -thick cap contact layer. Two different undoped SL were studied. Structure A consists of 14 periods of 17-Å $Al_{0.48}In_{0.52}As$/37-Å $Ga_{0.47}In_{0.53}As$. Structure B of 9 periods 23-Å $Al_{0.48}In_{0.52}As$/36-Å $Ga_{0.47}In_{0.53}As$. The layer thicknesses were verified by transmission electron microscopy. Circular mesas were wet-etched (diameter of the SL region $\approx$ 127 μm) and ohmic contacts were provided to the doped regions. The low background doping of the collector layer guarantees a uniform field across the SL length (<1000 Å) in the region of reverse bias of our experiments.

We modeled the SLs in the envelope function approximation taking into account energy-band nonparabolicity.[17] In structure A the calculated ground state miniband dispersion is $\Delta E_A \approx 115$ meV and its bottom lies at $E_0^A \approx 130$ meV while in structure B, $\Delta E_B \approx 80$ meV and $E_o^B \approx 154$ meV. Therefore, in order to inject electrons into the miniband, the composition of the p-doped quaternary layer was chosen to be $Al_{0.163}Ga_{0.312}In_{0.525}As$. Assuming a linear x-dependence for the $Al_xGa_{0.475-x}In_{0.525}As/Ga_{0.47}In_{0.53}As$ conduction band discontinuity, this corresponds to a conduction band offset of $\approx$ 180 meV, roughly the center of the minibands (see Fig. 2). The thickness of this layer is such that all the emitter electrons thermalize before impinging on the SL. Note

that for both samples, the ground-state miniband is wide enough to ensure the absence of localization due to fluctuations.[18] Moreover, the large energy separation ($\Delta E_s \approx 200$ meV in both samples) between the ground and first excited minibands insures that Zener tunneling will not be possible in our structures for $F < \Delta E_s/eL \approx 30$ kV/cm (for both samples), where L is the total length of the SL.

The collector current density as a function of the collector-junction bias at constant emitter current is shown in Fig. 3 for both samples. (The amplified scale has been chosen to clearly show the structure presented by the curves. The initial steeply rising region shows no features.) No space charge effects are present in our structure. In fact, by taking into account the electron velocity in the miniband regime,[6] one obtains an upper limit for the carrier density in the low 10^{13} cm^{-3}. Moreover, this is proved by the experimental fact that by varying the emitter current and therefore the electron flux incident on the SL, the collector current is simply scaled while the voltage positions of the relevant features are not altered. The current monotonically decreases in a wide bias range. As discussed above, this is the experimental manifestation of localization. It constitutes its first direct observation in a transport measurement. The threshold for the onset of NDC can be accurately determined by subtracting the collector-junction dark current to the measured characteristics; it is $F \approx 3$ kV/cm, for both samples.[19] This value is consistent with Eq. 1 taking $\tau \approx 4\times10^{-13}$ s, an adequate value for intrasubband scattering time[20] at these low fields.[20] This threshold value is much lower (a factor of 10) than the

minimum field required for interminiband tunneling, as required for the observability of NDC.[1] It should also be noted that intervalley transfer is not compatible with the experimental value for the NDC threshold. In $Ga_{0.47}In_{0.53}As$, which constitutes the largest portion of the collector, both theoretical[21] and experimental[22] values for the threshold field of intervalley transfer are $\sim$ 10 kV/cm, more than three times our experimental value.[23] Moreover the threshold for transfer will be even higher in our SL due to the presence of the $Al_{0.48}In_{0.52}As$ regions. The slope continues to be negative for fields corresponding to wavefunction confinement over few ($\sim$3-4 for both samples) wells where the characteristics exhibit a minimum.

The presence of the minimum indicates that, at sufficiently high bias, other paths can enhance electronic transport and become dominant in our structure. Firstly, an exponentially increasing Fowler-Nordheim current through the SL seen as an effective medium is to be expected.[24] More importantly, on this monotonically increasing background, several peaks are observed. To understand their physical origin, let us recall that in this field range, new states can arise from the mixing between Stark-ladder states originally belonging to different minibands or between the latter and resonances in the classical continuum above the SL barriers. In the case of transport in a SL without collision, these transmission resonances are determined by the whole SL. In the presence of collisions, however, they are determined by subsets of the SL of thickness equal to the electron coherence length. This is illustrated in Fig. 2b where one such state is shown for sample A. The electron coherence length must

therefore be explicitly considered and can be included through the electron mean free path λ. In fact, the fraction of electrons that will tunnel coherently for exactly n periods of the SL is equal to $e^{-\frac{ns}{\lambda}}(1-e^{-\frac{s}{\lambda}})$, and the corresponding transmission will be indicated by $T_n(F)$. The overall transmission coefficient is therefore given by:

$$T(F) = \sum_{n=1}^{n_T-1} e^{-\frac{ns}{\lambda}}\left(1 - e^{-\frac{s}{\lambda}}\right) T_n(F) + e^{-\frac{n_T s}{\lambda}} T_{n_T}(F), \qquad (3)$$

where n_T is the total number of wells. A fraction 1-T(F) of the impinging electrons are therefore reflected back into the p-doped layer and recombine. The remaining electrons are injected into the SL. Their "history" after the first scattering event is immaterial since in our steady-state situation all electrons injected into the SL reach the collector contact. Excellent agreement is found between calculated and experimental position of the peaks with $\lambda \approx 300$ Å. The calculated (experimental) biases for sample A are 5.6 (5.5), 6.7 (6.7), 8.5 (8.5), 10.9 V (10.9 V); for sample B 7.1 (7.1), 9.3 V (9.3 V). λ is obviously F-dependent, but we found that our results do not change appreciably with λ in the range 200-400 Å. On the contrary allowing for an infinite coherence length (i.e., electrons traversing ballistically the entire SL) leads to a much larger number of calculated resonances. As mentioned above, band nonparabolicities were included, the nonparabolicity parameter γ was taken equal to 1.7×10^{-18} m^2.[25]

It is important to note the connection between our results and the optical

experiments of Mendez et al.[10] These authors observed transitions between conduction-band states of spatial extent equal to the coherence length and totally localized valence-band states. These conduction-band states are the same that in our experiments give rise to the transmission resonances.

In conclusion, we have studied and modeled the properties of perpendicular transport in heterojunction SLs. Esaki-Tsu and field-induced localization have been analyzed critically. Their physical equivalence has been discussed and verified experimentally. At high fields, the dominant role of scattering-selected resonances has been presented and modeled.

The authors gratefully acknowledge stimulating discussions with A. S. Vengurlekar.

REFERENCES

[1] L. Esaki, and R. Tsu, IBM J. Res. Develop. **14**, 61 (1970). Later, with a different theoretical approach, the same phenomenon was studied by M. Büttiker and H. Thomas, Phys. Rev. Lett. **38**, 78 (1977).

[2] F. Capasso, S. Datta, Physics Today **43**, 74 (1990).

[3] P. A. Lebwohl, and R. Tsu, J. Appl. Phys. **41**, 2664 (1970).

[4] R. Tsu, and G. Döhler, Phys. Rev. **B12**, 680 (1975).

[5] G. Döhler, R. Tsu and L. Esaki, Solid State Commun. **17**, 317 (1975).

[6] F. Capasso, K. Mohammed, and A. Y. Cho, IEEE J. Quantum Electron **QE-22**, 1853 (1986).

[7] A. Sibille, J. F. Palmier, H. Wang, and F. Mollot, Phys. Rev. Lett. **64**, 52 (1990).

[8] G. Wannier, Phys. Rev. **117**, 432 (1960).

[9] R. F. Kazarinov and R. A. Suris, Fiz. Tekh. Poluprov. **5**, 797 (1971) [Sov. Phys. Semicond. **5**, 707 (1971)]; R. F. Kazarinov, and R. A. Suris, Fiz. Tekh. Poluprov. **6**, 148 (1972) [Sov. Phys. Semicond. **6**, 120 (1972)].

[10] E. E. Mendez, F. Agullo-Rueda, and J. M. Hong, Phys. Rev. Lett. **60**, 2426 (1988); F. Agullo-Rueda, E. E. Mendez, and J. M. Hong, Phys. Rev. **B 40**, 1357 (1989).

[11] P. Voisin, J. Bleuse, C. Bouche, S. Gaillard, C. Alibert, and A. Regreny, Phys. Rev. Lett. **61**, 1639 (1988).

[12] The approximate equivalence between $eaF > \hbar/\tau$ and $\lambda > \Delta E/eF$ where λ is the mean free path, is easily shown by noting that $\lambda \approx (\frac{\Delta E a}{\hbar})\tau$, where the term within brackets represents the average group velocity in the miniband.

[13] V. A. Yakolev, Fiz. Tverd. Tela **3**, 1983 (1962) [Sov. Phys. Solid State **3**, 1442 (1962)].

[14] Previously negative photoconductivity in 2-terminal SL structures was tentatively attributed to field-induced localization in the sense of Tsu and Döhler (Ref. 4). R. Tsu, L. L. Chang, A. Sai-Halasz, and L. Esaki, Phys. Rev. Lett. **34**, 1509 (1975); F. Capasso, K. Mohammed, and A. Y. Cho Physica B&C **134B**, 487 (1985).

[15] L. Esaki and L. L. Chang, Phys. Rev. Lett. **33**, 495 (1974).

[16] K. K. Choi, B. F. Levine, R. J. Malik, J. Walker, C. G. Bethea, Phys. Rev. **B 35**, 4172 (1987).

[17] D. F. Nelson, R. C. Miller, and D. A. Kleinman, Phys. Rev. **B 24**, 7720 (1987).

[18] F. Capasso, K. Mohammed, A. Y. Cho, R. Hull, and A. L. Hutchinson, Phys. Rev. Lett. **55**, 1152 (1985).

[19] The field in the SL is $F=(V+V_{bi})/L$, where L is the width of the intrinsic collector region and the built-in potential $V_{bi} \approx 0.92$ V.

[20] D. C. Herbert, Semicond. Sci. Technol. **3**, 101 (1988).

[21] M. E. Levinshtein, Fiz. Tekh. Poluprovodn. **13**, 1249 (1979) [Sov. Phys. Semicond. **13**, 735 (1979)].

[22] Y. Takeda, N. Shikagawa, and A. Sasaki, Solid St. Electron. **23**, 1003 (1980).

[23] It should also be noted that intervalley transfer does not manifest itself with NDC in conditions of constant current injection, as is well known by the theory of operation of bipolar transistors. In these conditions, in fact, the decrease in velocity caused by the lower mobility of the satellite valleys is compensated by an increase in the carrier density; their product (the current) is therefore not altered.

[24] The reverse-bias leakage current of the collector junction is negligible in the bias and temperature range of our experiments.

[25] Experimental measurements on γ give results in a rather broad range, $\gamma = 1.3\times10^{-18}$ m^2 was reported by L. Eaves, F. W. Sheard, G. A. Toombs, in *Physics of Quantum-Electron Devices*, edited by F. Capasso (Springer, New York, 1990); a value four times higher was found by C. K. Sarkar, R. J. Nicholas, J. C. Portal, M. Razeghi, J. Chevrier and J. Massies, J. Phys. C **18**, 2667 (1985). The value indicated was chosen to optimize the fit.

FIGURE CAPTIONS

Fig. 1. Schematic conduction-band diagram of a heterojunction superlattice with an applied field, (a) electronic states extend over several periods and can be broadened by scattering into a band (shaded region) if Eq. 1 is not satisfied, (b) at very high biases (defined by Eq. 2), electronic states are confined to single wells.

Fig. 2. (a) Energy-band diagram (not to scale) of the samples studied, (b) Conduction-band diagram of sample A at a bias such that a quasi-state supported by a subset of the superlattice of thickness equal to the electron coherence length enhances electronic transport. The solid curve represents the calculated wavefunction corresponding to the peak at 10.9 V.

Fig. 3 Collector current density as a function of the collector bias at constant emitter current ($I_E = 0.39$ A/cm^2) for samples A (top) and B (bottom). Both measurements were performed at T = 15 K. The features presented by the characteristics were visible up to temperatures as high as 200 K. The arrows indicate the calculated bias positions of the resonances.

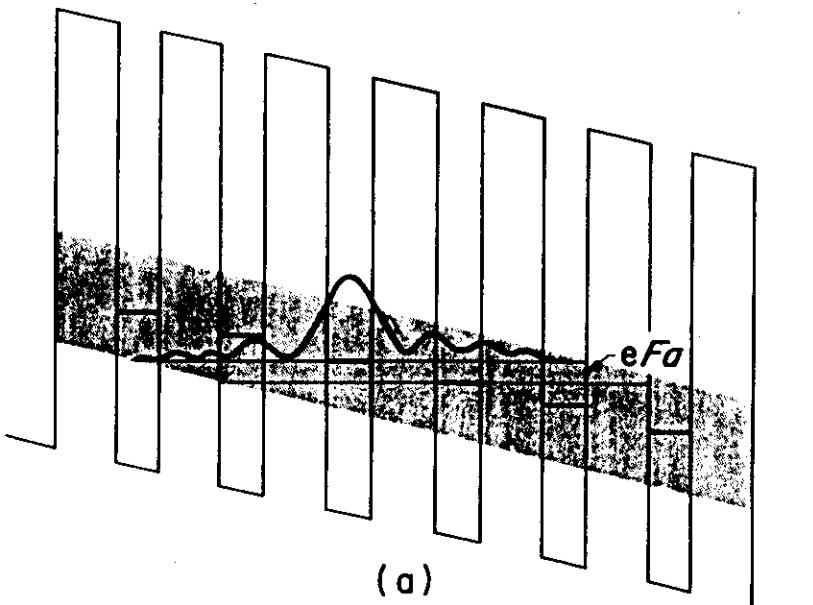

(a)

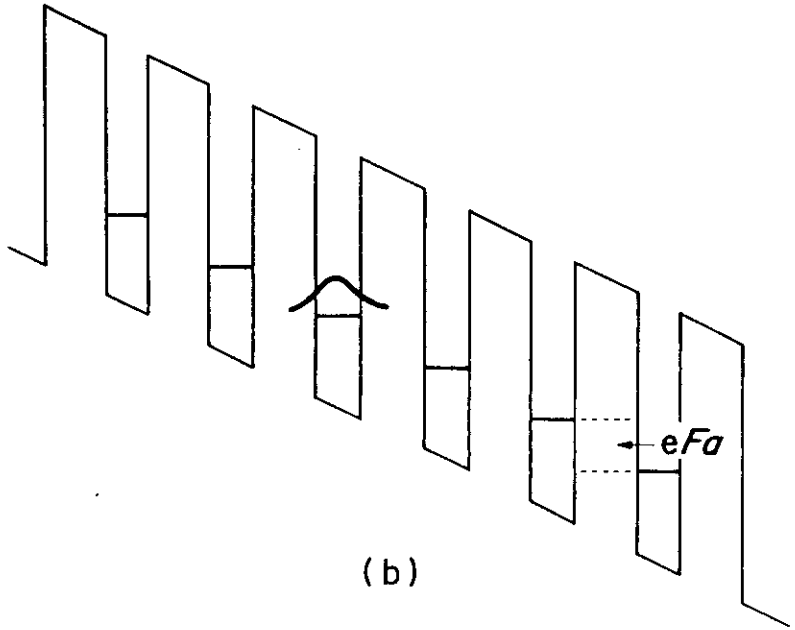

(b)

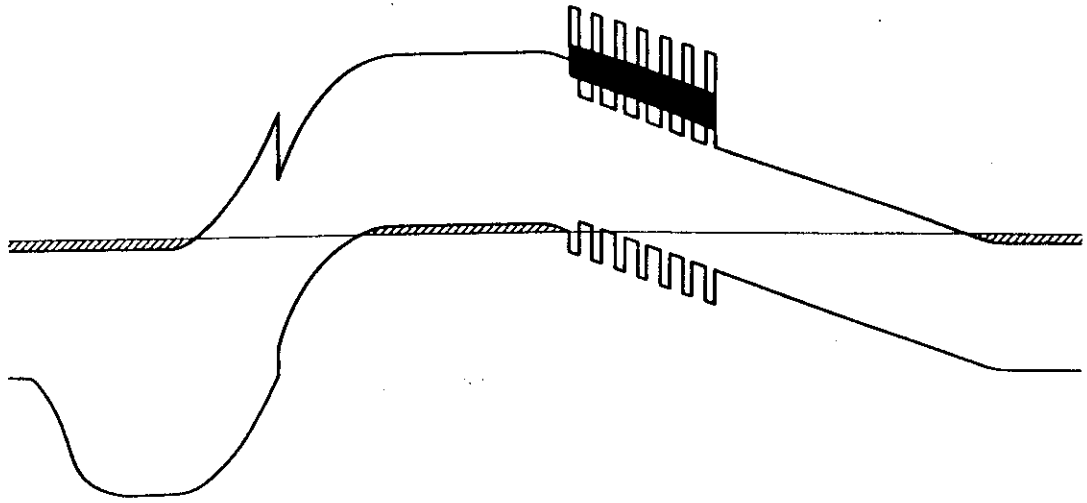

(a)

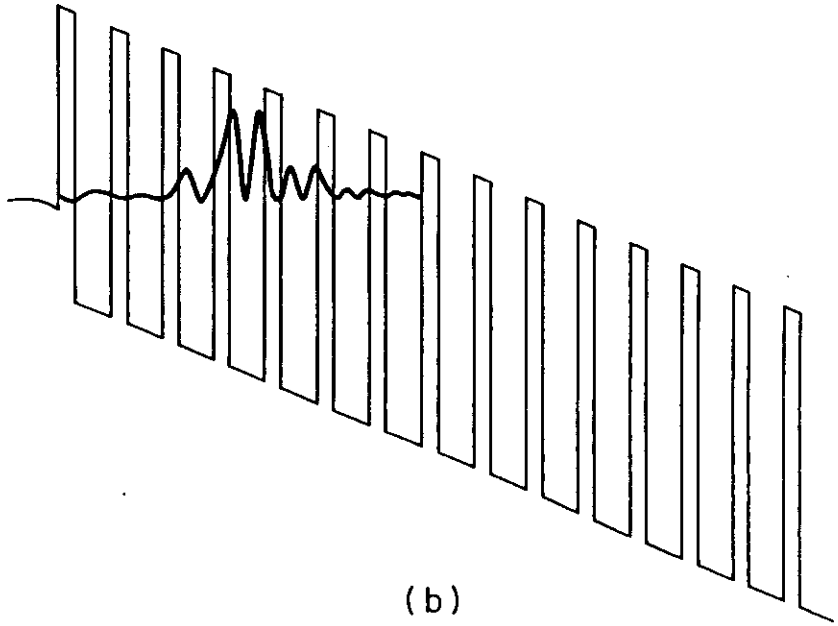

(b)

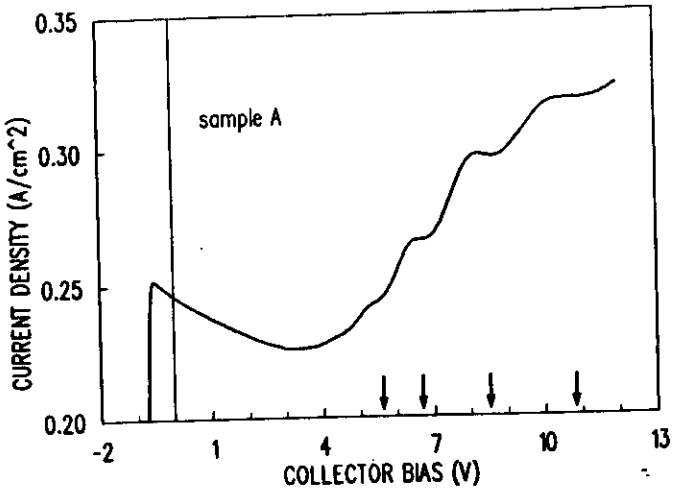
0.35
0.30
0.25
0.20
CURRENT DENSITY (A/cm^2)
sample A
-2
1
4
7
10
13
COLLECTOR BIAS (V)

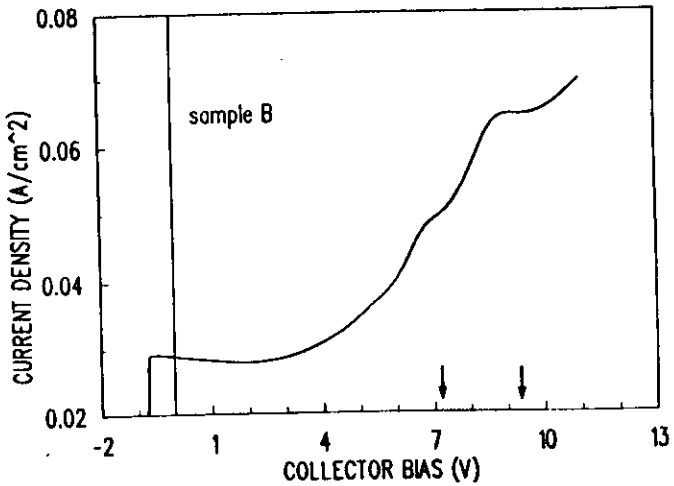
0.08
0.06
0.04
0.02
CURRENT DENSITY (A/cm^2)
sample B
-2
1
4
7
10
13
COLLECTOR BIAS (V)